

# A broadband cavity-enhanced spectrometer for atmospheric trace gas measurements and Rayleigh scattering cross sections in the cyan region (470-540 nm)

5 Nick Jordan,<sup>1</sup> Connie Z. Ye,<sup>1</sup> Satyaki Ghosh,<sup>1</sup> Rebecca A. Washenfelder,<sup>2</sup> Steven S. Brown,<sup>2</sup> and Hans D. Osthoff<sup>1</sup>

<sup>1</sup> Department of Chemistry, University of Calgary, 2500 University Drive NW, Calgary, AB T2N 1N4, Canada

<sup>2</sup> Earth System Research Laboratory, National Oceanic and Atmospheric Administration, 325 Broadway, Boulder,  
10 CO 80303, USA

*Correspondence:* Hans D. Osthoff (hosthoff@ucalgary.ca)

**Abstract.** An incoherent broadband cavity-enhanced absorption spectrometer (IBBCEAS) instrument for quantification of atmospheric trace gases that absorb in the cyan region of the electromagnetic spectrum (470 to 540 nm), including NO<sub>2</sub> and I<sub>2</sub>, is described. The instrument uses a light-emitting diode coupled to a 1 m optical cavity  
15 consisting of a pair of mirrors in stable resonator configuration. Transmitted light is monitored using a grating spectrometer and charge-coupled device array detector. The average mirror reflectivity was determined from the N<sub>2</sub>/He and Ar/He ratios of scattering coefficients and was ~99.98% at its maximum, yielding an effective optical path length of 6.3 km. Cross-sections of N<sub>2</sub>, O<sub>2</sub>, air, Ar, CO<sub>2</sub>, and CH<sub>4</sub> scattering and of O<sub>4</sub> absorption were measured and agree with literature values within the measurement uncertainty. Trace gas mixing ratios were retrieved using the  
20 spectral fitting software DOASIS from 480 to 535 nm. Under laboratory conditions, the 60 s, 1 $\sigma$  measurement precisions were  $\pm 124$  and  $\pm 44$  pptv for NO<sub>2</sub> and I<sub>2</sub>, respectively. The IBBCEAS instrument sampled ambient air in Ucluelet, BC, in July 2015. IBBCEAS retrievals agreed with independent measurements of NO<sub>2</sub> by blue diode laser cavity ring-down spectroscopy ( $r^2 = 0.975$ ), but ambient I<sub>2</sub> concentrations were below the detection limit.

## 25 1 Introduction

Cavity-enhanced absorption spectroscopy (CEAS) has emerged in recent years as a sensitive technique for direct measurement of atmospheric trace gases (Fiedler et al., 2003; Gherman et al., 2008; Vaughan et al., 2008; Washenfelder et al., 2008; Schuster et al., 2009; Thalman and Volkamer, 2010; Hoch et al., 2014) and of aerosol optical extinction (Thalman and Volkamer, 2010; Bluvshstein et al., 2012; Washenfelder et al., 2013). Similar to other  
30 cavity-enhanced techniques (Gagliardi and Loock, 2014), CEAS owes its high sensitivity to highly reflective mirrors (reflectivity,  $R > 99.9\%$ ) which yield long effective absorption path lengths. In CEAS, light generated from a high intensity broad-band light source (e.g., a Xe arc lamp) is transmitted through an optical cavity set up in a stable resonator configuration. The output spectrum is integrated yielding extinction spectra from which mixing ratios are retrieved using known absorption spectra and knowledge of the mirror reflectivity and effective optical absorption  
35 path (Meinen et al., 2010). To date, CEAS instruments have been used to quantify mixing ratios of many

atmospherically important trace gases, including nitrogen dioxide ( $\text{NO}_2$ ) (Langridge et al., 2008; Gherman et al., 2008; Triki et al., 2008; Thalman and Volkamer, 2010; Wu et al., 2014; Min et al., 2016; Varma et al., 2009), the nitrate radical ( $\text{NO}_3$ ) (Langridge et al., 2008; Schuster et al., 2009; Venables et al., 2006; Varma et al., 2009), iodine ( $\text{I}_2$ ) (Ball et al., 2010; Dixneuf et al., 2009; Bahrini et al., 2018), the iodine oxides IO and OIO (Vaughan et al., 2008), glyoxal (HCOHCO) (Washenfelder et al., 2008; Thalman and Volkamer, 2010; Coburn et al., 2014; Min et al., 2016), methyl glyoxal ( $\text{CH}_3\text{COCHO}$ ) (Thalman and Volkamer, 2010; Thalman et al., 2015; Min et al., 2016), molecular bromine ( $\text{Br}_2$ ), bromine monoxide (BrO) (Chen and Venables, 2011; Hoch et al., 2014), formaldehyde (Washenfelder et al., 2016), and nitrous acid (HONO) (Gherman et al., 2008; Wu et al., 2014; Min et al., 2016).

The accuracy of retrievals depends on knowledge of relevant absorption and scattering (i.e., Rayleigh) cross-sections (which both contribute to the optical extinction) and of the mirror reflectivity. Because of its high sensitivity, CEAS in turn has been utilized to measure these parameters. For example, Axson et al. and Kahan et al. recently reported the absorption cross-sections of  $\text{O}_3$  and  $\text{H}_2\text{O}_2$  (Axson et al., 2011; Kahan et al., 2012), and Thalman and Volkamer reported scattering cross-sections of  $\text{N}_2$ ,  $\text{O}_2$ , Ar, and air (Thalman and Volkamer, 2010) for several wavelength intervals (345 – 390, 435 – 490, 515 – 545, 560 – 600, and 600 – 700 nm).

In spite of the large number of CEAS instruments that have been constructed, the mid-visible region has received relatively little attention to date, other than the pioneering study by Vaughan et al. (2008), even though the absorption maxima of several key atmospheric traces gases, such as  $\text{NO}_2$  and the iodine species  $\text{I}_2$ , IO and OIO, are located in this wavelength interval (Figure 1). The study of iodine chemistry has been of considerable interest due to potential effects on the formation of new particles and atmospheric oxidising capacity through, for example, catalytic destruction of  $\text{O}_3$ , altering the partitioning of  $\text{NO}_x$  ( $= \text{NO} + \text{NO}_2$ ) and  $\text{HO}_x$  ( $= \text{HO} + \text{HO}_2$ ), or the activation of chlorine and bromine from sea salt aerosol in the marine and polar boundary layer, near salt lakes and volcanoes, and in the stratosphere (Saiz-Lopez et al., 2012). Prior laboratory measurements by Vaughan et al. used a 150 W Xenon arc lamp; such light sources tend to flicker, i.e., exhibit intensity fluctuations, which add noise to the absorption spectrum. For this and other reasons (such as compactness, heat generation, etc.), light-emitting diodes (LEDs) are now commonly used to generate broad-band radiation (Washenfelder et al., 2008; Min et al., 2016).

In this paper, we describe an LED-powered incoherent broadband cavity-enhanced absorption spectroscopy (IBBCEAS) instrument operated in the cyan region of the electromagnetic spectrum. We report laboratory measurements of scattering cross-sections for  $\text{N}_2$ ,  $\text{O}_2$ , Ar,  $\text{CO}_2$ ,  $\text{CH}_4$  and air from 480 to 535 nm and demonstrate detection of  $\text{NO}_2$  and  $\text{I}_2$  in laboratory-generated air. The IBBCEAS instrument was operated during the Ozone-depleting Reactions in a Coastal Atmosphere (ORCA) field campaign, conducted July 8-31, 2015 at the Amphitrite Point Observatory (APO) in Ucluelet on the west coast of Vancouver Island, British Columbia (Tokarek et al., 2017). Kelp forests are present along this coast line (Watson and Estes, 2011), which are expected to emit  $\text{I}_2$  (Dixneuf et al., 2009; Nitschke et al., 2015; Nitschke et al., 2011). Mixing ratios of  $\text{NO}_2$  retrieved from the cyan IBBCEAS data are compared to those measured by a co-located blue diode laser cavity ring-down spectrometer. The potential of the instrument for quantification of iodine species in laboratory and field experiments is assessed.

## 2 Theory

## 2.1 Cavity-enhanced spectroscopy

The principle of broadband trace gas measurements by IBBCEAS has been described elsewhere (Fiedler et al., 2003; Washenfelder et al., 2008). Briefly, broadband radiation is continuously injected and trapped between a set of highly  
 75 reflective mirrors forming a stable resonant cavity. The integrated cavity output intensity represents the combined extinction by the mirrors and the intra cavity medium. The absorption coefficient,  $\alpha_{abs}(\lambda)$ , is given in terms of the transmission signal through the cavity (Washenfelder et al., 2008) by Eq. (1):

$$\alpha_{abs}(\lambda) = R_L \left( \frac{1-R(\lambda)}{d} + \alpha_{Ray}(\lambda) \right) \left( \frac{I_0(\lambda)-I(\lambda)}{I(\lambda)} \right) \quad (1)$$

Here,  $R_L$  (see Sect. 3.3) is the ratio of the cell length ( $d \approx 102$  cm) divided by the length occupied by the sample ( $d_0 \approx$   
 80 82 cm - section 3.3),  $R(\lambda)$  is the average wavelength dependent mirror reflectivity,  $d$  is the distance between the two reflective surfaces (i.e. the cavity length),  $\alpha_{Ray}(\lambda)$  is the sum of all Rayleigh scattering sample constituents,  $I_0(\lambda)$  is the intensity spectrum in the absence of absorbers in the cavity cell, and  $I(\lambda)$  is the intensity spectrum measured in the presence of absorbers. When measurements are carried out in variable pressure environments (e.g., aircraft altitude change), an additional term ( $\Delta\alpha_{Ray}(\lambda)$ ) is added to Eq. (1) to account for pressure fluctuations (Min et al., 2016). If  
 85 multiple absorbers are present in the cavity, the absorption coefficient becomes the sum of all species expressed as in Eq. (2) (Washenfelder et al., 2008).

$$\alpha_{abs} = \sum_i^n \alpha_i(\lambda) = \sum_i^n N_i \sigma_i(\lambda, T, p) \quad (2)$$

Here,  $\sigma_i(\lambda, T, p)$  is the wavelength, temperature, and pressure-dependent absorption cross-section, and  $N_i$  is the number density of the  $i^{\text{th}}$  absorbing gas.

## 90 2.3 Determination of Rayleigh scattering cross-sections

Cavity-enhanced spectroscopic techniques allow accurate and precise measurements of Rayleigh scattering cross-sections of pure gases over broad wavelength regions (Naus and Ubachs, 2000; Sneep and Ubachs, 2005; Axson et al., 2011; Kahan et al., 2012; Thalman et al., 2014). If the mirror reflectivity  $R(\lambda)$  is known, the scattering cross-section of any gas can be determined by measuring its extinction and that of a reference gas (Thalman et al., 2014), e.g., for  
 95 CO<sub>2</sub> and using He as a reference:

$$\alpha_{Ray}^{CO_2}(\lambda) = \left( \left( \frac{1-R(\lambda)}{d} \right) \left( 1 - \frac{I_{CO_2}(\lambda)}{I_{He}(\lambda)} \right) + \alpha_{Ray}^{He}(\lambda) \right) \left( \frac{I_{He}(\lambda)}{I_{CO_2}(\lambda)} \right) \quad (3)$$

Here,  $\alpha_{Ray}(\lambda)$  is the optical extinction (in cm<sup>-1</sup>) caused by the intra-cavity scattering medium. The scattering cross-sections are then calculated through division by the number density of the gas ( $N_{gas}$ ), i.e.,

$$\sigma_{Ray}(\lambda) = \frac{\alpha_{Ray}(\lambda)}{N_{gas}} \quad (4)$$

100 Scattering cross-sections can be predicted if the refractive index,  $n$ , of a gas is known (Naus and Ubachs, 2000; Sneep and Ubachs, 2005), hereafter referred to as an " $n$ -based" cross-section,  $\sigma_n$ :

$$\sigma_n(\nu) = \frac{24\pi^3\nu^4}{N^2} \left( \frac{n^2(\nu)-1}{n^2(\nu)+1} \right)^2 F_k(\nu) \quad (5)$$

Here,  $\nu$  is the frequency in wavenumbers ( $\text{cm}^{-1}$ ),  $n(\nu)$  is the frequency dependent refractive index of the gas, and  $F_k$  is the King depolarization ratio which describes the effect of molecular anisotropy (King, 1923).

## 105 **3 Experimental**

### **3.1 Description of the IBBCEAS instrument**

The IBBCEAS instrument consists of an LED light source, collimating optics, a high finesse optical cavity, focusing optics, specialized fibre bundle, and a spectrograph equipped with a charge-coupled device (CCD) camera (Figure 2). The optical cavity consists of two dielectric-coated, plano-concave fused silica substrate mirrors (Advanced Thin  
 110 Films, Boulder, CO, USA) with maximum reflectivity from 460 to 550 nm, 2.54 cm in diameter, 0.635 cm thickness, and 1 m radius of curvature. To span a broad wavelength range, the mirrors were coated with two highly reflective substrates, resulting in a double maximum in their reflectivity. The mirrors were mounted on both ends of a 102 cm long cell with a gas sampling region of  $\sim 73$  cm and housed in a custom-built mount equipped with purge gas ports. A flow of 50 standard cubic centimeters per minute (sccm) of ultrapure air ("zero" grade, Praxair) set using 50  $\mu\text{m}$  critical  
 115 orifices (Lenox Laser, Glen Arm, MD, USA) and a gas regulator back pressure of 138 kPa was directed to each mirror to protect the optical surfaces from contamination. The mirror mounts were attached to adjustable kinematic mounts (Newport U200-A, Irvine, CA, USA) each equipped with 3 set screws for mirror alignment. The gas sampling region was enclosed using 1.9 cm outer diameter (o.d.) and 1.59 cm inner diameter (i.d.) fluorinated ethylene propylene (FEP) Teflon™ tubing (Saint Gobain Plastics, Chemfluor series). The Teflon™ tube was held in place by a custom  
 120 enclosure constructed from Aluminium. Gases entered and exited the sampling region through 1.9 cm o.d. perfluoroalkoxy alkane (PFA) Teflon™ fittings (Entegris Fluid Handling, Billerica, MA, USA). The LED (Thorlabs M505L3, Newton, NJ, USA; 400 mW nominal output power) output was collimated into the cavity by a single  $f/0.8$  aspheric condenser lens (Thorlabs ACL2520U-A). The cavity output was collected and focused by a 2.5 cm diameter  $f/1$  lens through a non-polarizing quartz beam splitter (Thorlabs BS025) onto a 0.5 cm (diameter)  
 125  $f/4$  fibre adapter that couples the radiation into a 2 m long 0.22 numerical aperture (NA) fibre bundle (Thorlabs BFL200HS02). The beam splitter has 90% transmission efficiency in the plane parallel to the cavity and 10% in the orthogonal plane and was used to direct the emission lines of a Hg(Ne) spectral calibration lamp (Newport Oriel 6032) towards the detector for calibration of the spectrometer wavelength scale and line width. The fibre bundle consists of  $7 \times 200 \mu\text{m}$  optical fibres arranged with circular and linear configurations on the input and output, respectively. The  
 130 fibre bundle output was oriented linearly along the spectrograph entrance slit to optimize coupling of the cavity output similar to (Min et al., 2016; Washenfelder et al., 2016), and illuminated the full vertical dimension of the CCD. Spectra were acquired by a 150 cm focal length  $f/4$  dual grating Czerny-Turner spectrograph (Princeton Instruments Acton SP2156, Trenton, NJ, USA) which back-illuminates a 16-bit  $1340 \times 100$  pixel CCD array (Princeton Instruments, PIXIS 100B), mounted at the focal plane of the spectrograph and Peltier-cooled to  $-80^\circ\text{C}$  to reduce thermal noise. The  
 135 spectrograph was configured with a  $1200 \text{ groove mm}^{-1}$  grating blazed at 500 nm. This configuration along with the

grating positioned at 500 nm central wavelength yielded spectral coverage from 446.9 to 563.2 nm spanning a total of 1340 discrete wavelength points. The Acton SP2156 spectrograph shipped with a mechanical shutter, which was removed in lieu of software control of the integration time via LABVIEW™ (National Instruments, Austin TX, USA). A fixed entrance slit width of 50 μm yielded approximately Gaussian profiles of the atomic Hg emission lines with full-width at half maximum (FWHM) of (0.330±0.003) nm at 540.06 nm. Other spectral lines (e.g., 520.39 nm) showed slightly lower resolution of roughly (0.360±0.016) nm (Figure S1). An integration time of 5-6 s saturated the CCD pixels 80–90% of their well depth near 500 nm.

All mechanical and optical components were mounted on an optical breadboard (Thorlabs MB2448) bolted onto aluminium structural rails (80/20, Columbia City, IN, USA). The net weight of the instrument including the breadboard and railing is < 90 kg and the overall power consumption below 300 W.

The IBBCEAS instrument samples air through a 47 mm diameter, circular, permeable polytetrafluoroethylene (PTFE) Teflon™ membrane filter with 1 μm pore size (Pall Teflon™ Series, Port Washington, NY, USA) housed in a PFA Teflon™ filter holder (Cole-Parmer R-06621-40) and through 0.635 cm outer diameter and 0.476 cm FEP Teflon™ tubing. The sample flow was set using a mass flow controller (MFC, MKS Instruments 100 B series, 15 standard litres per minute (slpm) capacity, Andover, MA, USA) connected to a diaphragm pump (KNF Neuberger UNO26.1.2ATP, Trenton, NJ, USA). The sample flow was in the range 1.5–2.5 slpm resulting in a sample residence time of 5.9–3.5 s. The gas temperature was measured using a K-type thermocouple (Omega, Laval, QC, Canada) attached to the aluminium sample cell enclosure. Pressure was measured using a pressure transducer (MKS Baratron capacitance manometer 722B) mounted on the exhaust portion of the IBBCEAS between the gas sample cell and the MFC.

The light source is a small footprint (1×1 mm) broadband LED (M505L3, Thorlabs) mounted on the end of a heat sink supplied by the manufacturer. We modified this assembly by mounting a Peltier module (CUI Inc. CP30238, Tualatin, Oregon, USA) between the LED and the heat sink for temperature control using a proportional–integral–derivative (PID) controller (Omega CNi3253) to 30.0±0.1 °C. If not stabilized, the LED output red-shifted ~0.1 nm per °C temperature change. The LED was operated just below the maximum current of 1000 mA (3.3 W of electrical power).

The LED output spectrum was characterized by an asymmetric shape, an emission maximum at 507.5 nm, and a peak width of 22.5 nm FWHM, and was a good match with the mirror reflectivity curve (Figure 3).

### 3.2 Determination of the mirror reflectivity

The response of the IBBCEAS instrument depends on  $R(\lambda)$  and  $d_0$  (Eq. (1)), which need to be accurately known. If an optical cavity is filled with a non-absorbing and inert gas, and aerosol are removed by filtering, the optical extinction is due to gas scattering only. In this case,  $R(\lambda)$  can be derived from the extinction caused by two individual gases with known and different scattering cross-sections such as N<sub>2</sub> and He (Washenfelder et al., 2008):

$$R(\lambda) = 1 - d \frac{\alpha_{Ray}^{N_2}(\lambda) \frac{I_{N_2}(\lambda)}{I_{He}(\lambda)} - \alpha_{Ray}^{He}(\lambda)}{1 - \frac{I_{N_2}(\lambda)}{I_{He}(\lambda)}} \quad (6)$$

170 Here,  $I_X(\lambda)$  and  $\alpha_{Ray}^X(\lambda)$  are the intensities and extinction coefficients of N<sub>2</sub> and He, respectively. Other pairs (e.g., He and Ar) may be used as well. For this work, we chose scattering cross-sections from (Peck and Khanna, 1966) for N<sub>2</sub>, (Cuthbertson and Cuthbertson, 1932) for He, and (Peck and Fisher, 1964) for Ar. Typically, combinations with He provide a higher signal-to-noise due to He having a much smaller scattering cross-section than other gases (Thalman et al., 2014). The above approach assumes that scattering and absorption within the optical cavity are small (Washenfelder et al., 2008) and neglects absorption and scattering due to the mirror substrate.

175 To determine  $R(\lambda)$  in this work, the cavity output intensity was recorded when the cell was filled with high purity N<sub>2</sub> (99.998%) or with He (99.998%) to atmospheric pressure (~890 hPa). In each case, the gases were delivered from a compressed gas cylinder (Praxair) and continuously injected through the purge ports until all other sample cell constituents were displaced through the open inlet port. To corroborate the results, the cavity was also filled with Ar (99.998%), which has slightly larger scattering cross-sections than that of N<sub>2</sub>.

180 Figure 3a shows cavity-enhanced transmission spectra with the optical cavity filled with N<sub>2</sub>, He, and Ar, each averaged over a 15 min time period. The intensity difference due to scattering by Ar and N<sub>2</sub> was more pronounced in the case when the sample cell was filled with He (Figure 3a, inset), as expected based on their relative cross-sections (Thalman et al., 2014).

185 Figure 3b shows the reflectivity spectra calculated using Eq. (6). The reflectivity curves are essentially smooth continua, with maximum reflectivity of ~99.98%. The relative difference between the reflectivity calculated from the ratios of Ar/He and N<sub>2</sub>/He was  $< 1.6 \times 10^{-6}$  in the 480–530 nm range. Arbitrarily, the N<sub>2</sub>/He mirror curve was chosen to calculate the mirror reflectivity for the remaining data analysis in this work with the exception of the scattering cross-sections of N<sub>2</sub> and CO<sub>2</sub> (see Sect. 4.1.1 and 4.1.5) for which the Ar/He pair was used. The observed reflectivity corresponds to a total path length ( $\approx d/(1-R)$ ) of 5.5 and 6.3 km near 485 nm and 520 nm, respectively. Intermittent measurements of mirror reflectivity showed that it remained unchanged throughout this work; in particular, no difference in reflectivity was found prior to and following the ORCA campaign.

190 The overall uncertainty in the measured mirror reflectivity was  $\pm 2.3\%$ , resulting from addition by quadrature of a  $\pm 1\%$  uncertainty in the N<sub>2</sub> scattering cross-section (Peck and Khanna, 1966), a  $\pm 2\%$  uncertainty in the He cross-section (Washenfelder et al., 2008; Min et al., 2016),  $\pm 0.4\%$  uncertainty in temperature,  $\pm 0.1\%$  uncertainty in pressure, and  $\pm 0.1\%$  random noise due to photon counting statistics.

### 3.3 Determination of the effective optical absorption path

200 When sampling ambient air, knowledge of the path length over which sampled air is present ( $d_0$ ) and the associated correction factor  $R_L$  is essential for accurate IBBCEAS measurements when purge gases are used to maintain clean mirrors as in this work. The effective cavity length,  $d_0$ , was determined by sampling pure oxygen and monitoring the O<sub>2</sub> dimer (Duan et al., 2018). This experiment was performed in the 350 - 390 nm wavelength region using highly reflective mirrors and an LED (Thorlabs M365LP1) suitable for this wavelength region, though in principle it could have been performed in the cyan region as well since both spectral regions contain O<sub>4</sub> absorption lines. Following Duan et al. (2018),  $d_0$  is given by

$$d_0 = d \times \frac{[O_2]_{on}}{[O_2]_{off}} \quad (7)$$

205 where  $[O_2]_{on}$  and  $[O_2]_{off}$  are the  $[O_2]$  retrieved using cross-sections by (Thalman and Volkamer, 2013) with or without the purge flows. Consistent results were obtained when a constant mixing ratio of  $NO_2$  was sampled (and purge flows were turned on and off) and from the ratio of expected absorption by  $O_4$  (calculated from the square of the number density of  $O_2$  and the  $O_4$  cross-section) relative to the observed  $O_4$  absorption, though the latter may be less accurate as the absorption changes non-linearly in the region where purge and sample gases mix and requires accurate knowledge of mirror reflectivity.

210 At a sample flow rate of 2.0 slpm, a purge flow rate of 0.1 slpm, and cell pressure of 870 hPa, we determined  $R_L = d/d_0 = 1.28 \pm 0.05$  ( $1\sigma$  precision stated) with an accuracy of  $\pm 5\%$ . This  $R_L$  value is smaller than calculated from the ratio of the inter-mirror distance  $d$  to the distance between the inlet and outlet of the sample flow ( $\sim 1.39$ ), which suggests that sampled air partially mixes into the purge volume. At a volumetric flow rate of 11 liters per minute as deployed during ORCA, we observed  $R_L = 1.20 \pm 0.07$  ( $1\sigma$  precision).

### 3.4 Reference absorption cross-sections

Figure 1 shows trace absorbers in the 480–530 nm window calculated as extinction ( $\alpha_i(\lambda) = \sigma_i(\lambda)N$ ) for typical atmospheric mixing ratios. CEAS analysis was performed using the high-resolution  $NO_2$  absorption cross-section of Voigt et al. (2002) and the cross-sections of Spietz et al. for OIO (Spietz et al., 2005) and  $I_2$  (Spietz et al., 2006), respectively. The  $NO_2$  cross-section was convolved with the instrument function corresponding to a sharp peak line (540.06 nm) in the emission spectrum of the Hg(Ne) calibration lamp (Figure S2), which was also used to calibrate the wavelength scale of the spectrometer.

225 The IBBCEAS instrument's resolution was 0.33 nm in the 480–530 nm window, whereas the  $NO_2$  literature spectrum was recorded at a higher resolution of better than 0.005 nm (Voigt et al., 2002). A convolved  $NO_2$  reference spectrum was used for the least-squares analysis. The literature cross-sections of  $I_2$  and OIO (Spietz et al., 2005; 2006) at a resolution of 0.59 nm were not convolved because their resolution was lower than that of the IBBCEAS instrument.

230 The  $NO_2$  absorption cross-section is somewhat pressure-dependent, which is important considering that the IBBCEAS instrument was operated at  $\sim 466$  hPa in the field. Voigt et al. (2002) reported cross-sections at 1333 and 133 hPa (in  $N_2$ ). Following convolution to the IBBCEAS instrument, these differences were judged to be small (2 – 5% in the 480 – 530 nm range).

### 3.5 Spectral fitting

The DOAS intelligent system (DOASIS; (Kraus, 2003)) was used to retrieve gas-phase concentrations. Optical extinction data collected in laboratory experiments were fitted using the literature absorption spectra (Sect. 3.3) and a third-degree polynomial to represent broad-band processes (e.g., temperature fluctuation, Mie scattering and extinction by aerosols). The "spectral shifting" setting in DOASIS was set to  $\pm 0.2$  nm, and stretching was disallowed.

The same parameters were used to fit the data from the ORCA field campaign except that in an effort to minimize the fit residuals, the convoluted absorption cross-section of H<sub>2</sub>O based on the high-resolution data by (Coheur et al., 2002) was also included in the fit. The contributions of water vapor to the optical extinction was small since the relative humidity of the air sampled during the background measurement was the same as during the measurement of NO<sub>2</sub> or I<sub>2</sub>. Further, the optical extinction ( $\alpha$ ) values, as per Eq. (1), were smoothed using a fourth order polynomial filter (Savitzky and Golay, 1964). Smoothing improved the root mean square (RMS) of the residuals and the fit uncertainty by a factor of ~2 (Figure S3).

### 3.6 Description of CRDS instrument

The IBBCEAS instrument quantified NO<sub>2</sub> in parallel to a blue diode laser CRDS instrument, which has been described previously (Paul and Osthoff, 2010; Odame-Ankrah, 2015). Briefly, mixing ratios of NO<sub>2</sub> are quantified by optical absorption using a continuous wave (cw) laser whose emission is centered at 405 nm (Power Technology IQ $\mu$ 2A105, Little Rock, AR, USA). The radiation is square-wave (on/off) modulated at a repetition rate of 1 kHz (50% duty cycle) and enters a 111 cm long stable resonator formed by two highly reflective mirrors (2.54 cm diameter; Advanced Thin Films, Boulder, CO, USA) in a concentric configuration. The cavity output is coupled into a 200  $\mu$ m diameter, 0.22 numerical aperture, multimode optical fibre (Thorlabs M25L01) illuminating a photomultiplier tube (Hamamatsu Photonics H9433-03MOD, Japan). The ring-down decay traces are co-added and fitted to an exponential using the discrete sums algorithm described by Everest and Atkinson (2008).

The CRDS NO<sub>2</sub> channel was operated in parallel to a CRDS NO<sub>x</sub> channel, to which a small flow of O<sub>3</sub> in O<sub>2</sub> was added to convert NO to NO<sub>2</sub>, similar to the method described by Fuchs et al. (2009). Following the O<sub>3</sub> addition point, the sampled air passed through a coiled reaction chamber with a total residence time of ~7 s to ensure complete titration and a linear response up to ~100 ppbv of NO (Odame-Ankrah, 2015). An identical chamber was added to the NO<sub>2</sub> channel to match the response times of the two channels. Mixing ratios of NO<sub>2</sub> and NO<sub>x</sub> measured by CRDS were accurate within  $\pm 10\%$  (Osthoff et al., 2017).

### 3.7 Generation and delivery of gases

Figure 2b shows the setup for delivery and sampling of NO<sub>2</sub>. NO<sub>2</sub> was generated by mixing the output of a standard NO cylinder (100.2 $\pm$ 1.0 ppmv in N<sub>2</sub>; Scott-Marrin, Riverside, CA, USA) delivered using a 20 sccm all metal MFC (MKS Instruments 1479A) with O<sub>3</sub> produced by illuminating a flow of O<sub>2</sub> (Praxair) with a 254 nm Hg pen-ray lamp (Jelight, Irvine, CA, USA) and dilution with zero air.

Iodine was purchased in a solid crystalline form ( $\geq 99.8\%$ , Sigma-Aldrich, Oakville, ON, Canada). Small amounts were placed in a Teflon™ permeation tube (VICI Metronics, Poulsbo, WA, USA); these tubes were sealed on both ends with PTFE plugs compressed with stainless steel rings and were (individually) placed in a temperature-controlled permeation chamber (Vici Metronics, model 120-1) operated with a constant air flow of ~0.3 litres per minute. The flow from the permeation chamber was diluted with zero air, yielding iodine concentrations in the range of ~70 pptv up to 21 ppbv depending on chamber temperature and permeation tube dimensions (i.e., wall thickness and length).

270 Ar, CO<sub>2</sub>, CH<sub>4</sub>, N<sub>2</sub>, O<sub>2</sub>, air and He were delivered from compressed gas cylinders (Praxair) in the same manner as described in section 3.2.

### 3.8 ORCA field campaign

The IBBCEAS instrument was operated alongside the CRDS during a four week long field intensive conducted at the Amphitrite Point Observatory (APO) on the west coast of Vancouver Island, British Columbia, Canada (Tokarek et al., 2017). The APO was established as a marine background monitoring site but is sporadically impacted by NO<sub>x</sub> emissions mainly from ship and boat traffic in the region (McKendry et al., 2014).

The IBBCEAS and CRDS instruments sampled, in parallel, from a 5.5 m long common 0.63 cm o.d. and 0.48 cm i.d. FEP Teflon™ inlet line, flooded with calibration gases and zero air at regular intervals. Zero air was generated using a custom-built zero air generation system (Odame-Ankrah, 2015), which delivered air at ambient relative humidity that was free of trace gases such as NO<sub>2</sub>, NO, I<sub>2</sub>, or O<sub>3</sub>. This approach minimized absorption by H<sub>2</sub>O from the extinction spectra which can create artifacts (Bahrini et al., 2018). A flow restriction was placed upstream of the inlet filter. When the IBBCEAS instrument was operated at a flow rate of 5 slpm, an average ( $\pm 1\sigma$ ) sample cell pressure of 473 ( $\pm 23$ ) hPa and inlet residence time of 2.3 s were achieved. The cell pressure varied over short time periods with a standard deviation of  $\pm 2.4$  hPa. A PAN-GC (Tokarek et al., 2014), commercial NO/NO<sub>y</sub> and O<sub>3</sub> instruments (Thermo 42i and 49i), as well as a 662 nm diode laser N<sub>2</sub>O<sub>5</sub> channel (Osthoff et al., 2017) also sampled off this common inlet line, resulting in all instruments periodically sampling a variety of calibration gases.

The IBBCEAS transmission spectrum was integrated for 9 s, resulting in ~90% saturation of the CCD at 500 nm. Dark spectra (to characterize the spectrometer offset) were acquired daily with the same integration time (9 s). Wavelength calibration spectra of the Hg(Ne) lamp were collected daily over a period of 2 min and showed that the spectrometer wavelength scale remained relatively unchanged ( $\pm 0.02$  nm) over the region of interest. The mirror reflectivity was measured prior to and after the campaign and agreed within  $\pm (1 \times 10^{-7})$ . Data were averaged over 60 s post-campaign prior to analysis.

## 4 Results

### 4.1 Measurements of cross-sections of pure gases

The extinction cross-sections of N<sub>2</sub>, CO<sub>2</sub> (based on mirror reflectivity determined from the Ar/He ratio of scattering coefficients), O<sub>2</sub>, air, Ar, and CH<sub>4</sub> (based on mirror reflectivity determined from the N<sub>2</sub>/He ratio of scattering coefficients) in the 480–535 nm wavelength range are shown in Figure 4; values at selected wavelengths are summarized in Table 1. For N<sub>2</sub>, Ar, and CO<sub>2</sub>, the extinction is due to scattering only. In contrast, the spectra of O<sub>2</sub>, air and CH<sub>4</sub> include optical losses due to absorption in addition to scattering. The systematic uncertainty of these data was  $\pm 2.5\%$ ; the systematic errors arise mainly from uncertainties in the mirror reflectivity ( $\pm 2.3\%$ , see Sect. 3.2) and errors in the scattering cross-section terms in Eq. (3). The precision of the data (calculated after subtracting a 4<sup>th</sup> order

polynomial from the observed cross-sections) varies from  $\pm 2.5\%$  for the  $\text{CO}_2$  data shown in Figure 4e to  $\pm 0.9\%$  for the  $\text{N}_2$  data shown in Figure 4b.

#### 305 **4.1.1 Nitrogen**

Figure 4b shows the measured scattering cross-sections of  $\text{N}_2$  at a temperature of  $299.0 \pm 0.1$  K and pressure of  $879.7 \pm 0.7$  hPa between 480 and 535 nm. Superimposed are  $n$ -based cross-sections predicted using Eq. (5), data by (Peck and Khanna, 1966), and the King correction factor by (Bates, 1984). In addition, the single wavelength CRDS measurement at 532.2 nm by (Sneep and Ubachs, 2005) and the nephelometer data of (Shardanand and Rao, 1977) are shown.

310 The IBBCEAS data are marginally larger than the  $n$ -based prediction, with the percent difference ranging from  $+0.2\%$  at 525.07 nm to  $+1.3\%$  at 485.03 nm (Table 1). These differences are well within the margin of measurement error ( $\pm 2.5\%$ ), set in this case by the accuracy of the scattering cross-sections of He ( $\pm 2\%$ ) and Ar ( $< 1\%$ ). The IBBCEAS data differ from the CRDS data of (Sneep and Ubachs, 2005) at 532.2 nm by  $+7.1\%$ , though the error bars overlap; 315 the measurement uncertainty of the CRDS data alone is  $\pm 9.4\%$ . The IBBCEAS measurements also differ by  $+4.6\%$  at 488.0 nm and by  $+8.8\%$  at 514.5 nm) from the data of (Shardanand and Rao, 1977) but are within combined measurement error ( $\pm 2.5\%$  and  $\pm 11\%$ , respectively).

#### **4.1.2 Argon**

320 The scattering cross-sections of Ar at  $299.0 \pm 0.1$  K and  $879.7 \pm 0.7$  hPa are shown in Figure 4b. Superimposed are the  $n$ -based cross-sections calculated using data from (Peck and Fisher, 1964) and the King correction factor from (Bates, 1984). The single-wavelength measurement of (Sneep and Ubachs, 2005) and the nephelometer data of (Shardanand and Rao, 1977) are shown for comparison.

The observed scattering cross-sections are marginally larger than the  $n$ -based prediction, by  $+1.3\%$  at shorter wavelengths and  $+0.21\%$  at 515.06 nm (Table 1). These differences are within measurement error of the IBBCEAS 325 instrument ( $\pm 2.5\%$ ) inferred from the accuracy in the determination of the scattering cross-sections of He ( $\pm 2\%$ ) and  $\text{N}_2$  ( $\pm 1\%$ ) used in the determination of the mirror reflectivity. The IBBCEAS cross-sections differ from the CRDS data by (Sneep and Ubachs, 2005) at 532.2 nm and are well within either measurement error bar (Figure 4b). In contrast, the CEAS values differ from the nephelometer data by  $-10.8\%$  at 488.0 nm and by  $-5.1\%$  at 514.5 nm, though they are within the  $\pm 11\%$  uncertainty of the nephelometer.

#### 330 **4.1.3 Oxygen**

The extinction cross-sections of  $\text{O}_2$  (at a temperature of 299 K and a pressure of 880 hPa) are shown in Figure 4c next to the  $n$ -based predictions based on (Bates, 1984) and the nephelometer measurements of (Shardanand and Rao, 1977). The IBBCEAS data show two absorption bands due to the oxygen dimer,  $\text{O}_4$ , centered at 477 nm and 532 nm (Thalman and Volkamer, 2013). In the 490 – 515 nm wavelength interval, the contribution of these absorption bands to the total

335 extinction is negligible (<0.2% at 515 nm), i.e., the extinction is dominated by scattering. In this region, the observed  
cross-sections are slightly larger than the *n*-based data of (Bates, 1984): the differences range from +8.3% at 495.08  
nm to +2.5% at 515.06 nm (Table 1). Relative to the nephelometer measurements, the IBBCEAS data differ by +8.7%  
at 488 nm and by +15.3% at 514.5 nm.

We calculated the absorption cross-section of O<sub>4</sub> by subtracting the scattering cross-section of (Bates, 1984), upshifted  
340 by  $+3.86 \times 10^{-28} \text{ cm}^2 \text{ molecule}^{-1}$  (i.e., by 6%) to match the *n*-based data to the observed extinction from 487 nm to  
516 nm, from the extinction shown in Figure 4c, and dividing by the number density of O<sub>2</sub> ( $2.13 \times 10^{19} \text{ molecules cm}^{-3}$ ).  
The result is shown in Figure S4. The error for this absorption cross-section calculation is estimated at  $\pm 8.5\%$ , with  
the largest source of error being the correction to the scattering cross-section extrapolated from the region where  
absorption is negligible. For the smaller band between 520 and 540 nm, the observed cross-section of  
345  $(1.08 \pm 0.09) \times 10^{-46} \text{ cm}^5 \text{ molecule}^{-2}$  is in agreement with recent room-temperature measurements by other groups (Table  
S1). For the larger band between 467 and 485 nm, the peak cross-section of  $(6.2 \pm 0.5) \times 10^{-46} \text{ cm}^5 \text{ molecule}^{-2}$  is smaller  
than that reported in recent measurements (Thalman and Volkamer, 2013; Sneep et al., 2006), though the shape of the  
peak is identical and the error bars overlap.

#### 4.1.4 Air

350 Figure 4d shows the extinction spectrum of ultrapure air ("zero" grade, Praxair) at a temperature of  $(298.5 \pm 0.1) \text{ K}$  and  
pressure of  $879.7 \pm 0.7 \text{ hPa}$ . Superimposed is the *n*-based prediction from the refractive index data of (Penndorf, 1957)  
and King correction factor from (Bodhaine et al., 1999).

The sample cylinder contains a sufficiently high quantity of O<sub>2</sub> (~19.5% by volume, Praxair) for O<sub>4</sub> absorption bands  
to appear at 477.5 and 531.5 nm. In the 495 - 515 nm wavelength region, the cross-sections observed by IBBCEAS  
355 are slightly larger than the *n*-based prediction, by +4.0%, +3.0%, and +6.8% at 495, 505, and 515 nm, respectively  
(Table 1).

#### 4.1.5 Carbon dioxide

Figure 4e shows the scattering cross-sections of CO<sub>2</sub> at  $(299.0 \pm 0.1) \text{ K}$  and  $(879.7 \pm 0.7 \text{ hPa})$  for the 475 – 540 nm  
wavelength interval. Superimposed are the *n*-based prediction based on (Bideau-Mehu et al., 1973), nephelometer  
360 measurements (Shardanand and Rao, 1977), and a CRDS measurement at 532.2 nm (Sneep and Ubachs, 2005). The  
observed scattering cross-sections differ from the *n*-based prediction by -2.9%, +2.4% and -2.8% at 485 nm, 505 nm,  
and 525 nm, respectively (Table 1). In contrast, the CRDS measurement at 532.2 nm, which has a relatively high  
uncertainty of  $\pm 6.5\%$  at the  $1\sigma$  level, is 11% lower than the IBBCEAS measurement. The nephelometer measurements  
(Shardanand and Rao, 1977), on the other hand, are significantly larger than the other data shown and appear to be in  
365 error.

#### 4.1.6 Methane

Figure 4f shows the extinction spectrum of CH<sub>4</sub> (research grade, 99.97%) for the 475 – 550 nm interval at (298.5±0.1) K and 879.7±0.7 hPa. The CH<sub>4</sub> spectrum in this region contains a number of combination and overtone absorption bands near 484.7, 486.1, 509.6, 522.0, and 543.4 nm that have been assigned by (Giver, 1978). These bands are relevant to studies simulating the atmospheres of Jovian planets (e.g., Uranus, Neptune) and Saturn’s moon Titan that contain CH<sub>4</sub> (Karkoschka, 1994). Superimposed are CRDS data by (Sneep and Ubachs, 2005) and the *n*-based scattering cross-sections, calculated using the parameterization by Sneep and Ubachs, and refractive index data from (Hohm, 1993), assuming a depolarization ratio of unity and nephelometer data by (Shardanand and Rao, 1977) extrapolated using Eq. (5) (dashed line). In spite of the many absorption bands, there are small windows where the optical extinction appears to be dominated by scattering and a comparison with literature is feasible. There is very little difference (within combined measurement errors) between IBBCEAS and interpolated nephelometer data at those wavelengths. At 492.06 nm and 527.28 nm, for example, the data are within -0.07% and 0.17%, respectively (Table 1). There is also reasonable agreement between the IBBCEAS and CRDS data 532.2 nm, which differ by 4.7% but compares well with the total IBBCEAS uncertainty of 4.6% for CH<sub>4</sub>.

## 380 4.2 Measurement of trace gas mixing ratios

### 4.2.1 Nitrogen dioxide

An example of a spectral retrieval for NO<sub>2</sub> in ambient air is shown on Figure 5a. The figure shows the measured optical extinction ( $\alpha$ ) for a routine calibration period during the ORCA campaign on 22 Jul 2015 at 11:52:07 to 11:57:02 (UTC). Superimposed is a fit determined with DOASIS. An NO<sub>2</sub> mixing ratio of (11.6 ± 0.4) ppbv was retrieved, corresponding to an ambient air mixing ratio of (13.9±1.0) ppbv when R<sub>L</sub> is factored in. The residual spectrum is lacking structure, indicating that other absorbers are not significant in this wavelength region.

During the ORCA campaign, the inlet of the IBBCEAS instrument (and of the CRDS instrument, which sampled in parallel) was overflowed every 30 min with a standard gas mixture of ~20 ppbv NO<sub>x</sub> containing up to 16 ppbv of NO<sub>2</sub> in zero air and with ~130 ppbv of NO added to ambient air. The zero air was generated using a scrubber constructed in-house that delivered air with a similar moisture content as ambient air. A subset of these data (and the ambient air data sampled in between) is shown in Figure 6a.

High concentrations of NO in air are prone to oxidation (by O<sub>3</sub> and, to a lesser degree, by O<sub>2</sub>) to NO<sub>2</sub> (Atkinson et al., 2004). Because the CRDS had a longer inlet residence time (7 s) than the IBBCEAS instrument (2.3 s), it observed greater conversion of NO to NO<sub>2</sub> when the high NO concentration standard was sampled in an ambient air matrix. On the other hand, when the lower concentration NO<sub>x</sub> standard was sampled in O<sub>3</sub>-free air, the two instruments were in better agreement (Figure 6a).

Shown in Figure 7a is a scatter plot of all of the NO<sub>x</sub> calibration data. This plot shows a linear relationship with a slope of 1.11±0.01, an intercept of 0.2±0.1 ppbv, and  $r^2 = 0.975$ . The slope of the line in Figure 7a reveals an 11% systematic difference in the measurement of the calibration standard.

400 The median NO<sub>2</sub> mixing ratio during ORCA was 1.24 ppbv. Shown in Figure 6b is a time series of a subset of ambient air NO<sub>2</sub> measurements. The IBBCEAS NO<sub>2</sub> data clearly exhibit more scatter than the CRDS NO<sub>2</sub> data and occasionally

fall below zero. For ambient air data collected on 18-19 Jul 2015, the scatter plot of IBBCEAS and CRDS NO<sub>2</sub> data (Figure 7b) has the same slope ( $1.12 \pm 0.02$ ) as that shown in Figure 7a, while the scatter plot of the entire campaign has a slope of  $1.02 \pm 0.01$  (Figure 7C). When data are filtered by removing all IBBCEAS points below a factor of three times the standard deviation of a blank measurement for 60 s ( $\sim 1$  ppbv; see Sect. 4.3), the slope of the scatter plot, when forced through an intercept of zero, is  $1.18 \pm 0.01$  ( $r^2 = 0.70$ ), suggesting that the IBBCEAS are biased high.

#### 4.2.2 Iodine species (I<sub>2</sub>, OIO)

Figure 5b shows an example retrieval for I<sub>2</sub>. The extinction spectrum was recorded during the ORCA campaign on 18 Jul 2015, when I<sub>2</sub> from a permeation source had been added to the inlet and represents a 60 s average. A mixing ratio of  $(10.1 \pm 0.2)$  ppbv was retrieved in this example.

Figure S5 shows spectra of laboratory generated I<sub>2</sub> samples and their respective absorption spectra, fits, and residuals. Fit results near 20 pptv showed large residuals ( $\pm 27\%$ ) indicating that the IBBCEAS instrument was near its detection limit.

A sample time series of laboratory I<sub>2</sub> measurements (30 s averaged data) is shown in Figure S6. Gas streams containing I<sub>2</sub> were generated using four permeation tubes of different wall thickness, that were exchanged while the output of the permeation was bypassed and the IBBCEAS sampled zero air. The IBBCEAS instrument responded rapidly to concentration changes: for example, at 22:05, the response 30 s after "zeroing" was 10% of the preceding value, indicating that memory effects (from slow adsorption / desorption kinetics of iodine on the inner walls of the inlet) were negligible.

Figure S7 shows a sample time series of I<sub>2</sub> mixing ratios during the ORCA campaign. Concentrations of I<sub>2</sub> (and of OIO, not shown) in ambient air were below the instrument's detection limits. At 22:30 UTC, I<sub>2</sub> from a diffusion source was added to the inlet. While the transmission of iodine through inlets was not systematically investigated in this work, the square-wave response and quick rise and fall times suggest the absence of inlet transmission losses.

#### 4.3 Accuracy and limits of detection

The accuracy of the IBBCEAS NO<sub>2</sub> measurement is influenced by uncertainties in the absorption cross-section of NO<sub>2</sub> ( $\pm 3\%$ ) (Voigt et al., 2002), fit errors  $\pm(3 - 5\%)$ , which can be reduced to  $\pm(2 - 4\%)$  by smoothing), scattering cross-sections, i.e., mirror reflectivity ( $\pm 2.5\%$ ; Sect. 3.2 and 4.1),  $R_L$  ( $\pm 5\%$ ; Sect. 3.3), and errors in the mass flow controller reading ( $\pm 1\%$ ), sample cell pressure readout ( $\pm 0.5\%$ ), and temperature measurement ( $\pm 0.7\%$ ). The total uncertainty, expressed as the square root of the individual errors summed in quadrature, is  $\pm(7 - 8\%)$ . Not included in this estimate are errors arising from interpolation of infrequent mirror reflectivity and  $R_L$  determinations in the field. The limits of detection (LOD) were assessed through Allan deviation analyses (Werle et al., 1993). For NO<sub>2</sub> sampled at a flow of 1.5 slpm and cell pressure of 890 hPa, the Allan deviation was  $\pm 360$  pptv for 10 s data,  $\pm 135$  pptv for 60

s data, and  $\pm 63$  pptv for 5 min data averages (Figure 8a). At the higher sample flow of 5 slpm and reduced cell pressure of 466 hPa used during the ORCA campaign, the Allan deviation was  $\pm 164$  pptv for 334 s data (Figure S8).

For  $I_2$  in laboratory-generated samples, typical  $1\sigma$  fit errors for 60 s averaged data were  $\pm 7$  pptv when 21 pptv  $I_2$  were sampled and  $\pm 9$  pptv when 544 pptv  $I_2$  were sampled (Figure S6). The accuracy of  $I_2$  data is, in principle, of similar magnitude to that of the  $NO_2$  data, except that it also depends on knowledge of inlet transmission efficiency, which was not assessed in this work. The Allan deviation plot in Figure 8b demonstrates  $1\sigma$  measurement precisions for  $I_2$  of  $\pm 49$  pptv for 60 s and  $\pm 22$  pptv for 5 min averaged data. During ORCA, the  $1\sigma$  precisions were  $\pm 120$  pptv for 60 s and  $\pm 60$  pptv for 5 min data, respectively.

For OIO, the Allan deviation analysis gives  $1\sigma$  measurement precisions of  $\pm 5.7$  pptv for 60 s and  $\pm 2.3$  pptv for 5 min averaged data (Figure S9b) in the laboratory.

## 5 Discussion

The IBBCEAS instrument described in this work adds to a growing number of instruments designed for measurement of atmospheric trace gases (Table 2). It differentiates itself foremost through its wavelength region, where several trace gases of atmospheric interest (e.g.,  $NO_2$ ,  $I_2$ , IO, and OIO) absorb (Figure 1). Measurements of optical absorption in the cyan region enable simultaneous quantification of  $I_2$ , and, potentially, IO, and OIO in a single channel. Currently, such measurements require multiple detection channels, for example quantification of  $I_2$  and OIO mixing ratios using the 525 – 555 nm range and those of IO the 420 – 460 nm window in a separate channel (Vaughan et al., 2008). A reduction of channels and LEDs corresponds to savings in space and power requirements, important considerations in the field.

As such, this paper has laid some of the ground work for future measurements in the cyan spectral region, in that we measured relevant scattering and absorption cross-sections of pure gases (see S.I.). Such information is needed to determine mirror reflectivity and is useful to probe the consistency of scattering cross-sections reported for this wavelength region (of which there have been relatively few) and, hopefully, improve upon their accuracy, to better describe transmission of radiation through the atmosphere.

Scattering cross-section measurements for non-absorbing gases agree with recent literature values (Figure 4 and Table 1). For example, the IBBCEAS scattering cross-section measurements agree, within the combined experimental uncertainties ( $1\sigma$ ), with the CRDS data by (Sneep and Ubachs, 2005) at 532.2 nm for  $N_2$ , Ar,  $CO_2$ , and  $CH_4$ , and with the nephelometer measurements of (Shardanand and Rao, 1977) at 488.0 and 514.5 nm for  $N_2$ , Ar,  $O_2$ , and  $CH_4$ . For  $CO_2$ , the IBBCEAS data closely match the data by (Bideau-Mehu et al., 1973) and recent data by (He et al., 2018); the older data by (Shardanand and Rao, 1977), in contrast, appear high (Figure 4e).

In the case of  $CH_4$ , to lesser extent,  $O_2$  and, air, the analysis is complicated by absorption lines. For  $O_2$ , our data and derived collisional-induced absorption cross-sections agree with literature (Table S1). For regions that appear to be free of absorption bands, the IBBCEAS data for  $CH_4$  (Figure 4f) agree with cross-section measurements of (Shardanand and Rao, 1977) but not with the more recent work of (Hohm, 1993) whose data appear high. The CRDS data point by (Sneep and Ubachs, 2005) is on a shoulder of a large absorption band and hence not a valid measurement of scattering but extinction cross-section; their data agrees with the extinction cross-section observed in this work.

470 Accurate knowledge of the scattering cross-section of CH<sub>4</sub> is important to the study of planetary bodies with atmospheric content of CH<sub>4</sub> such as Saturn's moon Titan. Future studies should re-examine the scattering cross-section measurements of CH<sub>4</sub> to resolve the reported differences.

The detection limit for NO<sub>2</sub> achieved under laboratory conditions in this work (63 pptv for 5 min data) is of similar magnitude as those by instruments operated in other wavelength regions (Table 2). However, the IBBCEAS measurement precision in this work was surpassed by the more mature blue diode CRDS, though future upgrades (see 475 below) may improve the IBBCEAS precision. On the other hand, the IBBCEAS may ultimately be more accurate. Unlike IBBCEAS where all absorbing molecules are incorporated in the fit, the measurement of NO<sub>2</sub> by blue diode laser CRDS is prone to potential interference from molecules that absorb at 405 nm such as glyoxal and methyl glyoxal (Fuchs et al., 2009). For example, Fuchs et al. estimated that the presence of glyoxal could introduce an interference 480 of ~1% in polluted and up to 10% in forested environments (Fuchs et al., 2009). The low precision of the data in the scatter plot shown in Figure 7c prevents us from drawing a definitive conclusion as to the magnitude of such interferences. Still, future comparisons of IBBCEAS and blue diode CRDS measurements of ambient NO<sub>2</sub> should be conducted. The data presented in this manuscript show that accurate measurements of NO<sub>2</sub> in ambient air by a cyan IBBCEAS are possible.

485 An important parameter in any IBBCEAS measurement is the effective cavity length. Duan et al. recently summarized past practices in its determination and found that these practices vary considerably between groups (Duan et al., 2018). In this work, the necessary correction ( $R_L = 1.28$  at 2.0 slpm sample flow rate) differed substantially from the physical dimension of the cell (1.39), underlining its importance for accurate measurements. However, it is unclear to what extent  $R_L$  varies between molecules which will need to be investigated. To improve the accuracy of future 490 measurements, we will deploy more frequent zeroing and verify  $R_L$  periodically, for example by periodic sampling of molecular oxygen and measuring O<sub>4</sub> concentration.

The sensitivity for I<sub>2</sub> and OIO (22 and 2.3 pptv for 5 min averaged data under laboratory conditions) suffices for their quantification in environmental chamber studies (Dixneuf et al., 2009). Further, these LODs are below maximum I<sub>2</sub> and OIO abundances reported at Mace Head, Ireland, of 94 and 13 pptv (Bitter et al., 2005) and 61 and 9.2 pptv (Peters et al., 2005), respectively, but above the maximum I<sub>2</sub> level of 4 pptv reported in California (Finley and Saltzman, 2008). This implies that iodine species on the West coast of British Columbia, Canada, might have been detected if the instrument had been operated optimally. Even then, the LOD for I<sub>2</sub> of ~100 pptv (2 $\sigma$ , 60 s average) is larger than the LOD of 26 pptv (2 $\sigma$ , 60 s average) reported by Vaughan et al. (2008). This suggests that improvements are possible. One area for improvement is the thermal management of the LED. Its intensity and wavelength drifts with temperature, 500 necessitating temperature stabilization to achieve a constant emission profile. In this work, the cyan LED was stabilized by mounting a single Peltier thermoelectric module and thermocouple between the heat sink and the LED. When evaluated in the climate-controlled laboratory, this yielded a cavity emission profile that varied along the entire wavelength range (446.9–563.2 nm) of the spectrometer by  $\pm 15$  counts (Figure S10). At 500 nm, this corresponded to an absorption coefficient of  $\pm 1 \times 10^{-9}$  cm<sup>-1</sup>. During the field deployment, however, the LED was subject to greater 505 output fluctuations, since the trailer temperature was not as well controlled as in the laboratory, and thermal gradients between the LED and thermocouple may have come into play.

When deployed in the field, the performance of the IBBCEAS instrument was also compromised by variable cell pressure which added noise to the optical extinction, caused in part by the large pressure drop from ~1013 to ~467 hPa. Furthermore, we discovered post-campaign that the alignment of the round-to-linear fiber bundle is very sensitive to vibrations, which would have added additional noise during the field campaign. In future deployments, improved pressure, temperature and vibrational stabilization of the sample cell (as it is common in aircraft deployments, for example) and instrument will be paramount.

### **Acknowledgments**

This work was made possible by the financial support of the Natural Science and Engineering Research Council of Canada (NSERC) in the form of a Discovery grant, of the Canadian Foundation for Innovation (CFI) in the form of a LOF grant, and by the Government of Alberta's Advanced Education and Technology (AET) Small Equipment Grants Program (SEGP). The authors thank the Birrs and Thurbide groups at the University of Calgary for loans of CH<sub>4</sub> and CO<sub>2</sub> compressed gas cylinders used in this work.

520 **References**

- Atkinson, R., Baulch, D. L., Cox, R. A., Crowley, J. N., Hampson, R. F., Hynes, R. G., Jenkin, M. E., Rossi, M. J., and Troe, J.: Evaluated kinetic and photochemical data for atmospheric chemistry: Volume I - gas phase reactions of O<sub>x</sub>, HO<sub>x</sub>, NO<sub>x</sub> and SO<sub>x</sub> species, *Atmos. Chem. Phys.*, 4, 1461-1738, 10.5194/acp-4-1461-2004, 2004.
- 525 Axson, J. L., Washenfelder, R. A., Kahan, T. F., Young, C. J., Vaida, V., and Brown, S. S.: Absolute ozone absorption cross section in the Huggins Chappuis minimum (350 - 470 nm) at 296 K, *Atmos. Chem. Phys.*, 11, 11581-11590, 10.5194/acp-11-11581-2011, 2011.
- Bahrini, C., Grégoire, A.-C., Obada, D., Mun, C., and Fittschen, C.: Incoherent broad-band cavity enhanced absorption spectroscopy for sensitive and rapid molecular iodine detection in the presence of aerosols and water vapour, *Optics & Laser Technology*, 108, 466-479, 10.1016/j.optlastec.2018.06.050, 2018.
- 530 Ball, S. M., Hollingsworth, A. M., Humbles, J., Leblanc, C., Potin, P., and McFiggans, G.: Spectroscopic studies of molecular iodine emitted into the gas phase by seaweed, *Atmos. Chem. Phys.*, 10, 6237-6254, 10.5194/acp-10-6237-2010, 2010.
- 535 Bates, D. R.: Rayleigh scattering by air, *Planetary and Space Science*, 32, 785-790, 10.1016/0032-0633(84)90102-8, 1984.
- Bideau-Mehu, A., Guern, Y., Abjean, R., and Johannin-Gilles, A.: Interferometric determination of the refractive index of carbon dioxide in the ultraviolet region, *Optics Communications*, 9, 432-434, 10.1016/0030-4018(73)90289-7, 1973.
- 540 Bitter, M., Ball, S. M., Povey, I. M., and Jones, R. L.: A broadband cavity ringdown spectrometer for in-situ measurements of atmospheric trace gases, *Atmos. Chem. Phys.*, 5, 2547-2560, 10.5194/acp-5-2547-2005, 2005.
- Bluvshstein, N., Flores, J. M., Riziq, A. A., and Rudich, Y.: An Approach for Faster Retrieval of Aerosols, *Complex Refractive Index Using Cavity Ring-Down Spectroscopy*, *Aerosol Sci. Technol.*, 46, 1140-1150, 10.1080/02786826.2012.700141, 2012.
- 545 Bodhaine, B. A., Wood, N. B., Dutton, E. G., and Slusser, J. R.: On Rayleigh optical depth calculations, *Journal of Atmospheric and Oceanic Technology*, 16, 1854-1861, 10.1175/1520-0426(1999)016<1854:ORODC>2.0.CO;2, 1999.
- Burkholder, J. B., and Talukdar, R. K.: Temperature-Dependence of the Ozone Absorption-Spectrum over the Wavelength Range 410 to 760 nm, *Geophys. Res. Lett.*, 21, 581-584, 10.1029/93GL02311, 1994.
- 550 Chen, J., and Venables, D. S.: A broadband optical cavity spectrometer for measuring weak near-ultraviolet absorption spectra of gases, *Atmos. Meas. Tech.*, 4, 425-436, 10.5194/amt-4-425-2011, 2011.
- 555 Coburn, S., Ortega, I., Thalman, R., Blomquist, B., Fairall, C. W., and Volkamer, R.: Measurements of diurnal variations and eddy covariance (EC) fluxes of glyoxal in the tropical marine boundary layer: description of the Fast LED-CE-DOAS instrument, *Atmos. Meas. Tech.*, 7, 3579-3595, 10.5194/amt-7-3579-2014, 2014.
- 560 Coheur, P. F., Fally, S., Carleer, M., Clerbaux, C., Colin, R., Jenouvrier, A., Merienne, M. F., Hermans, C., and Vandaele, A. C.: New water vapor line parameters in the 26000-13000 cm<sup>-1</sup> region, *J. Quant. Spectrosc. Radiat. Transf.*, 74, 493-510, 10.1016/S0022-4073(01)00269-2, 2002.

- Cuthbertson, C., and Cuthbertson, M.: The refraction and dispersion of neon and helium, P R Soc Lond a-Conta, 135, 40-47, 10.1098/rspa.1932.0019, 1932.
- 565 Dixneuf, S., Ruth, A. A., Vaughan, S., Varma, R. M., and Orphal, J.: The time dependence of molecular iodine emission from *Laminaria digitata*, Atmos. Chem. Phys., 9, 823-829, 10.5194/acp-9-823-2009, 2009.
- Duan, J., Qin, M., Ouyang, B., Fang, W., Li, X., Lu, K., Tang, K., Liang, S., Meng, F., Hu, Z., Xie, P., Liu, W., and Häsler, R.: Development of an incoherent broadband cavity-enhanced absorption spectrometer for in situ measurements of HONO and NO<sub>2</sub>, Atmos. Meas. Tech., 570 11, 4531-4543, 10.5194/amt-11-4531-2018, 2018.
- Everest, M. A., and Atkinson, D. B.: Discrete sums for the rapid determination of exponential decay constants, Rev. Sci. Instrum., 79, 023108-023109, 10.1063/1.2839918, 2008.
- Fiedler, S. E., Hese, A., and Ruth, A. A.: Incoherent broad-band cavity-enhanced absorption spectroscopy, Chem. Phys. Lett., 371, 284-294, 10.1016/s0009-2614(03)00263-x, 2003.
- 575 Finley, B. D., and Saltzman, E. S.: Observations of Cl<sub>2</sub>, Br<sub>2</sub>, and I<sub>2</sub> in coastal marine air, J. Geophys. Res., 113, D21301, 10.1029/2008jd010269, 2008.
- Fuchs, H., Dubé, W. P., Lerner, B. M., Wagner, N. L., Williams, E. J., and Brown, S. S.: A Sensitive and Versatile Detector for Atmospheric NO<sub>2</sub> and NO<sub>x</sub> Based on Blue Diode Laser Cavity Ring-Down Spectroscopy, Environm. Sci. Technol., 43, 7831-7836, 10.1021/es902067h, 2009.
- 580 Gagliardi, G., and Loock, H.-P.: Cavity-Enhanced Spectroscopy and Sensing, 1 ed., Springer Series in Optical Sciences, 179, Springer, Berlin, Heidelberg, 10.1007/978-3-642-40003-2, 2014.
- Gherman, T., Venables, D. S., Vaughan, S., Orphal, J., and Ruth, A. A.: Incoherent broadband cavity-enhanced absorption spectroscopy in the near-ultraviolet: Application to HONO and NO<sub>2</sub>, Environm. Sci. Technol., 42, 890-895, 10.1021/es0716913, 2008.
- 585 Giver, L. P.: Intensity measurements of the CH<sub>4</sub> bands in the region 4350 Å to 10,600 Å, J. Quant. Spectrosc. Radiat. Transfer, 19, 311-322, 10.1016/0022-4073(78)90064-X, 1978.
- He, Q., Bluvshstein, N., Segev, L., Meidan, D., Flores, J. M., Brown, S. S., Brune, W., and Rudich, Y.: Evolution of the Complex Refractive Index of Secondary Organic Aerosols during Atmospheric Aging, Environm. Sci. Technol., 52, 3456-3465, 10.1021/acs.est.7b05742, 2018.
- 590 Hoch, D. J., Buxmann, J., Sihler, H., Pöhler, D., Zetzsch, C., and Platt, U.: An instrument for measurements of BrO with LED-based Cavity-Enhanced Differential Optical Absorption Spectroscopy, Atmos. Meas. Tech., 7, 199-214, 10.5194/amt-7-199-2014, 2014.
- 595 Hohm, U.: Experimental determination of the dispersion in the main linear dipole polarizability  $\alpha(\omega)$  of small hydrocarbons and evaluation of Cauchy moments between 325 nm and 633 nm, Molecular Physics, 78, 929-941, 10.1080/00268979300100621, 1993.
- Kahan, T. F., Washenfelder, R. A., Vaida, V., and Brown, S. S.: Cavity-Enhanced Measurements of Hydrogen Peroxide Absorption Cross Sections from 353 to 410 nm, J. Phys. Chem. A, 116, 5941-5947, 10.1021/jp2104616, 2012.
- 600 Karkoschka, E.: Spectrophotometry of the Jovian Planets and Titan at 300- to 1000-nm Wavelength: The Methane Spectrum, Icarus, 111, 174-192, 10.1006/icar.1994.1139, 1994.
- King, L. V.: On the complex anisotropic molecule in relation to the dispersion and scattering of light, P R Soc Lond a-Conta, 104, 333-357, 10.1098/rspa.1923.0113, 1923.
- 605 Knight, G., Ravishankara, A. R., and Burkholder, J. B.: Laboratory studies of OBrO, J. Phys. Chem. A, 104, 11121-11125, 10.1021/jp002226u, 2000.

- Langridge, J. M., Ball, S. M., and Jones, R. L.: A compact broadband cavity enhanced absorption spectrometer for detection of atmospheric NO<sub>2</sub> using light emitting diodes, *Analyst*, 131, 916-922, 10.1039/B605636A, 2006.
- 610 Langridge, J. M., Ball, S. M., Shillings, A. J. L., and Jones, R. L.: A broadband absorption spectrometer using light emitting diodes for ultrasensitive, in situ trace gas detection, *Rev. Sci. Instrum.*, 79, 123110, 10.1063/1.3046282, 2008.
- McKendry, I. G., Christensen, E., Schiller, C., Vingarzan, R., Macdonald, A. M., and Li, Y.: Low Ozone Episodes at Amphitrite Point Marine Boundary Layer Observatory, British Columbia, Canada, *Atmosphere-Ocean*, 52, 271-280, 10.1080/07055900.2014.910164, 2014.
- 615 Meinen, J., Thieser, J., Platt, U., and Leisner, T.: Technical Note: Using a high finesse optical resonator to provide a long light path for differential optical absorption spectroscopy: CE-DOAS, *Atmos. Chem. Phys.*, 10, 3901-3914, 10.5194/acp-10-3901-2010, 2010.
- Min, K. E., Washenfelder, R. A., Dubé, W. P., Langford, A. O., Edwards, P. M., Zarzana, K. J., Stutz, J., Lu, K., Rohrer, F., Zhang, Y., and Brown, S. S.: A broadband cavity enhanced absorption spectrometer for aircraft measurements of glyoxal, methylglyoxal, nitrous acid, nitrogen dioxide, and water vapor, *Atmos. Meas. Tech.*, 9, 423-440, 10.5194/amt-9-423-2016, 2016.
- 620 Naus, H., and Ubachs, W.: Experimental verification of Rayleigh scattering cross sections, *Opt. Lett.*, 25, 347-349, 10.1364/ol.25.000347, 2000.
- Nitschke, U., Ruth, A. A., Dixneuf, S., and Stengel, D. B.: Molecular iodine emission rates and photosynthetic performance of different thallus parts of *Laminaria digitata* (Phaeophyceae) during emersion, *Planta*, 233, 737-748, 10.1007/s00425-010-1334-3, 2011.
- Nitschke, U., Dixneuf, S., Schmid, M., Ruth, A. A., and Stengel, D. B.: Contribution of living and degrading kelp to coastal iodine fluxes, *Mar. Biol.*, 162, 1727-1738, 10.1007/s00227-015-2699-4, 2015.
- 630 Odame-Ankrah, C. A.: Improved detection instrument for nitrogen oxide species, Ph.D., Chemistry, University of Calgary, <http://hdl.handle.net/11023/2006>, 10.5072/PRISM/26475, Calgary, 2015.
- 635 Osthoff, H. D., Odame-Ankrah, C. A., Taha, Y. M., Tokarek, T. W., Schiller, C. L., Haga, D., Jones, K., and Vingarzan, R.: Low levels of nitryl chloride at ground level: Nocturnal nitrogen oxides in the Lower Fraser Valley of British Columbia, *Atmos. Chem. Phys.*, 18, 6293-6315, 10.5194/acp-18-6293-2018, 2017.
- Paul, D., and Osthoff, H. D.: Absolute Measurements of Total Peroxy Nitrate Mixing Ratios by Thermal Dissociation Blue Diode Laser Cavity Ring-Down Spectroscopy, *Anal. Chem.*, 82, 6695-6703, 10.1021/ac101441z, 2010.
- 640 Peck, E. R., and Fisher, D. J.: Dispersion of argon, *Journal of the Optical Society of America*, 54, 1362-1364, 10.1364/josa.54.001362, 1964.
- Peck, E. R., and Khanna, B. N.: Dispersion of nitrogen, *Journal of the Optical Society of America*, 56, 1059-1063, 10.1364/josa.56.001059, 1966.
- 645 Penndorf, R.: Tables for the refractive index for standard air and the Rayleigh scattering coefficient for the spectral region between 0.2 and 20.0  $\mu$ m and their application to atmospheric optics, *Journal of the Optical Society of America*, 47, 176-182, 10.1364/josa.47.000176, 1957.

- 650 Peters, C., Pechtl, S., Stutz, J., Hebestreit, K., Honninger, G., Heumann, K. G., Schwarz, A.,  
Winterlik, J., and Platt, U.: Reactive and organic halogen species in three different European  
coastal environments, *Atmos. Chem. Phys.*, 5, 3357-3375, 10.5194/acp-5-3357-2005, 2005.
- Saiz-Lopez, A., Plane, J. M. C., Baker, A. R., Carpenter, L. J., von Glasow, R., Gómez Martín, J. C.,  
655 McFiggans, G., and Saunders, R. W.: Atmospheric Chemistry of Iodine, *Chem. Rev.*, 112,  
1773-1804, 10.1021/cr200029u, 2012.
- Savitzky, A., and Golay, M. J. E.: Smoothing and Differentiation of Data by Simplified Least  
Squares Procedures, *Anal. Chem.*, 36, 1627-1639, 10.1021/ac60214a047, 1964.
- Schuster, G., Labazan, I., and Crowley, J. N.: A cavity ring down/cavity enhanced absorption  
device for measurement of ambient NO<sub>3</sub> and N<sub>2</sub>O<sub>5</sub>, *Atmos. Meas. Tech.*, 2, 1-13,  
660 10.5194/amt-2-1-2009, 2009.
- Shardanand, and Rao, A. D. P.: Absolute Rayleigh scattering cross sections of gases and freons  
of stratospheric interest in the visible and ultraviolet regions, NASA TN D-8442, 1977.
- Sneep, M., and Ubachs, W.: Direct measurement of the Rayleigh scattering cross section in  
various gases, *J. Quant. Spectrosc. Radiat. Transfer*, 92, 293-310,  
665 10.1016/j.jqsrt.2004.07.025, 2005.
- Sneep, M., Ityaksov, D., Aben, I., Linnartz, H., and Ubachs, W.: Temperature-dependent cross  
sections of O<sub>2</sub>-O<sub>2</sub> collision-induced absorption resonances at 477 and 577 nm, *J. Quant.  
Spectrosc. Radiat. Transf.*, 98, 405-424, 10.1016/j.jqsrt.2005.06.004, 2006.
- Spietz, P., Gómez Martín, J. C., and Burrows, J. P.: Spectroscopic studies of the I<sub>2</sub>/O<sub>3</sub>  
670 photochemistry: Part 2. Improved spectra of iodine oxides and analysis of the IO absorption  
spectrum, *J. Photochem. Photobiol. A*, 176, 50-67, 10.1016/j.jphotochem.2005.08.023, 2005.
- Spietz, P., Gómez Martín, J., and Burrows, J. P.: Effects of column density on I<sub>2</sub> spectroscopy and  
a determination of I<sub>2</sub> absorption cross section at 500 nm, *Atmos. Chem. Phys.*, 6, 2177-2191,  
10.5194/acp-6-2177-2006, 2006.
- 675 Thalman, R., and Volkamer, R.: Temperature dependent absorption cross-sections of O<sub>2</sub>-O<sub>2</sub>  
collision pairs between 340 and 630 nm and at atmospherically relevant pressure, *Phys.  
Chem. Chem. Phys.*, 15, 15371-15381, 10.1039/c3cp50968k, 2013.
- Thalman, R., Zarzana, K. J., Tolbert, M. A., and Volkamer, R.: Rayleigh scattering cross-section  
measurements of nitrogen, argon, oxygen and air, *J. Quant. Spectrosc. Radiat. Transfer*, 147,  
680 171-177, 10.1016/j.jqsrt.2014.05.030, 2014.
- Thalman, R., Baeza-Romero, M. T., Ball, S. M., Borrás, E., Daniels, M. J. S., Goodall, I. C. A.,  
Henry, S. B., Karl, T., Keutsch, F. N., Kim, S., Mak, J., Monks, P. S., Muñoz, A., Orlando, J.,  
Peppe, S., Rickard, A. R., Ródenas, M., Sánchez, P., Seco, R., Su, L., Tyndall, G., Vázquez, M.,  
Vera, T., Waxman, E., and Volkamer, R.: Instrument intercomparison of glyoxal, methyl  
685 glyoxal and NO<sub>2</sub> under simulated atmospheric conditions, *Atmos. Meas. Tech.*, 8, 1835-1862,  
10.5194/amt-8-1835-2015, 2015.
- Thalman, R. M., and Volkamer, R. M.: Inherent calibration of a blue LED-CE-DOAS instrument to  
measure iodine oxide, glyoxal, methyl glyoxal, nitrogen dioxide, water vapour and aerosol  
extinction in open cavity mode, *Atmos. Meas. Tech.*, 3, 1797-1814, 10.5194/amt-3-1797-  
690 2010, 2010.
- Tokarek, T. W., Huo, J. A., Odame-Ankrah, C. A., Hammoud, D., Taha, Y. M., and Osthoff, H. D.: A  
gas chromatograph for quantification of peroxy-carboxylic nitric anhydrides calibrated by

- thermal dissociation cavity ring-down spectroscopy, *Atmos. Meas. Tech.*, 7, 3263-3283, 10.5194/amt-7-3263-2014, 2014.
- 695 Tokarek, T. W., Brownsey, D. K., Jordan, N., Garner, N. M., Ye, C. Z., Assad, F. V., Peace, A., Schiller, C. L., Mason, R. H., Vingarzan, R., and Osthoff, H. D.: Biogenic emissions and nocturnal ozone depletion events at the Amphitrite Point Observatory on Vancouver Island, *Atmosphere-Ocean*, 55, 121-132, 10.1080/07055900.2017.1306687, 2017.
- 700 Triki, M., Cermak, P., Méjean, G., and Romanini, D.: Cavity-enhanced absorption spectroscopy with a red LED source for NO<sub>x</sub> trace analysis, *Applied Physics B: Lasers and Optics*, 91, 195-201, 10.1007/s00340-008-2958-x, 2008.
- Varma, R. M., Venables, D. S., Ruth, A. A., Heitmann, U., Schlosser, E., and Dixneuf, S.: Long optical cavities for open-path monitoring of atmospheric trace gases and aerosol extinction, *Appl. Optics*, 48, B159-B171, 10.1364/AO.48.00B159, 2009.
- 705 Vaughan, S., Gherman, T., Ruth, A. A., and Orphal, J.: Incoherent broad-band cavity-enhanced absorption spectroscopy of the marine boundary layer species I<sub>2</sub>, IO and OIO, *Phys. Chem. Chem. Phys.*, 10, 4471-4477, 10.1039/b802618a, 2008.
- Venables, D. S., Gherman, T., Orphal, J., Wenger, J. C., and Ruth, A. A.: High sensitivity in situ monitoring of NO<sub>3</sub> in an atmospheric simulation chamber using incoherent broadband cavity-enhanced absorption spectroscopy, *Environm. Sci. Technol.*, 40, 6758-6763, 10.1021/es061076j, 2006.
- 710 Voigt, S., Orphal, J., and Burrows, J. P.: The temperature and pressure dependence of the absorption cross-sections of NO<sub>2</sub> in the 250-800 nm region measured by Fourier-transform spectroscopy, *Journal Of Photochemistry And Photobiology A-Chemistry*, 149, 1-7, 10.1016/S1010-6030(01)00650-5, 2002.
- 715 Washenfelder, R. A., Langford, A. O., Fuchs, H., and Brown, S. S.: Measurement of glyoxal using an incoherent broadband cavity enhanced absorption spectrometer, *Atmos. Chem. Phys.*, 8, 7779-7793, 10.5194/acp-8-7779-2008, 2008.
- 720 Washenfelder, R. A., Flores, J. M., Brock, C. A., Brown, S. S., and Rudich, Y.: Broadband measurements of aerosol extinction in the ultraviolet spectral region, *Atmos. Meas. Tech.*, 6, 861-877, 10.5194/amt-6-861-2013, 2013.
- 725 Washenfelder, R. A., Attwood, A. R., Flores, J. M., Zarzana, K. J., Rudich, Y., and Brown, S. S.: Broadband cavity-enhanced absorption spectroscopy in the ultraviolet spectral region for measurements of nitrogen dioxide and formaldehyde, *Atmos. Meas. Tech.*, 9, 41-52, 10.5194/amt-9-41-2016, 2016.
- Watson, J., and Estes, J. A.: Stability, resilience, and phase shifts in rocky subtidal communities along the west coast of Vancouver Island, Canada, *Ecol. Monogr.*, 81, 215-239, 10.1890/10-0262.1, 2011.
- 730 Werle, P., Mucke, R., and Slemr, F.: The Limits of Signal Averaging in Atmospheric Trace-Gas Monitoring by Tunable Diode-Laser Absorption-Spectroscopy (TDLAS), *Applied Physics B-Photophysics and Laser Chemistry*, 57, 131-139, 10.1007/BF00425997, 1993.
- Wu, T., Zha, Q., Chen, W., Xu, Z., Wang, T., and He, X.: Development and deployment of a cavity enhanced UV-LED spectrometer for measurements of atmospheric HONO and NO<sub>2</sub> in Hong Kong, *Atmos. Environm.*, 95, 544-551, 10.1016/j.atmosenv.2014.07.016, 2014.
- 735

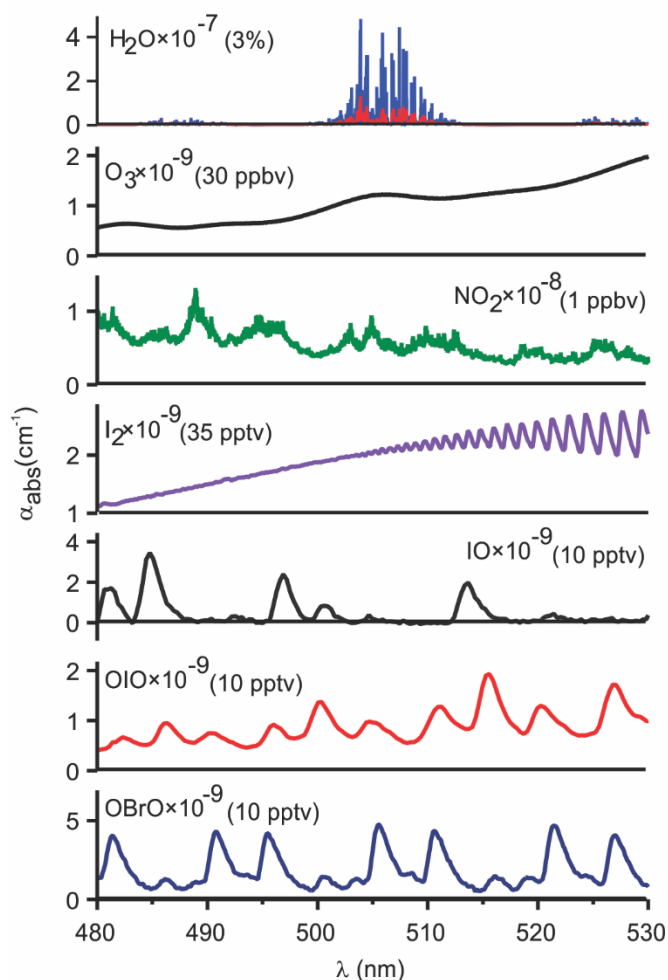


**Figure 1.** Absorption coefficients for atmospheric absorbers in the cyan region at typical tropospheric mixing ratios (stated in brackets after each species). Absorption cross-sections were downloaded from the Max-Planck Institute for Chemistry's web site located at <http://www.uv-vis-spectral-atlas-mainz.org> and are based on the following:  $\text{H}_2\text{O}$  (Coheur et al., 2002),  $\text{O}_3$  (Burkholder and Talukdar, 1994),  $\text{NO}_2$  (Voigt et al., 2002),  $\text{I}_2$  (Spietz et al., 2006),  $\text{IO}$ ,  $\text{OIO}$  (Spietz et al., 2005), and  $\text{OBrO}$  (Knight et al., 2000). The literature cross-sections for  $\text{H}_2\text{O}$  (shown in blue) were convolved with the resolution of the IBBCEAS (shown in red). The absorption cross-section of  $\text{O}_4$  is shown in Figure S4.

745

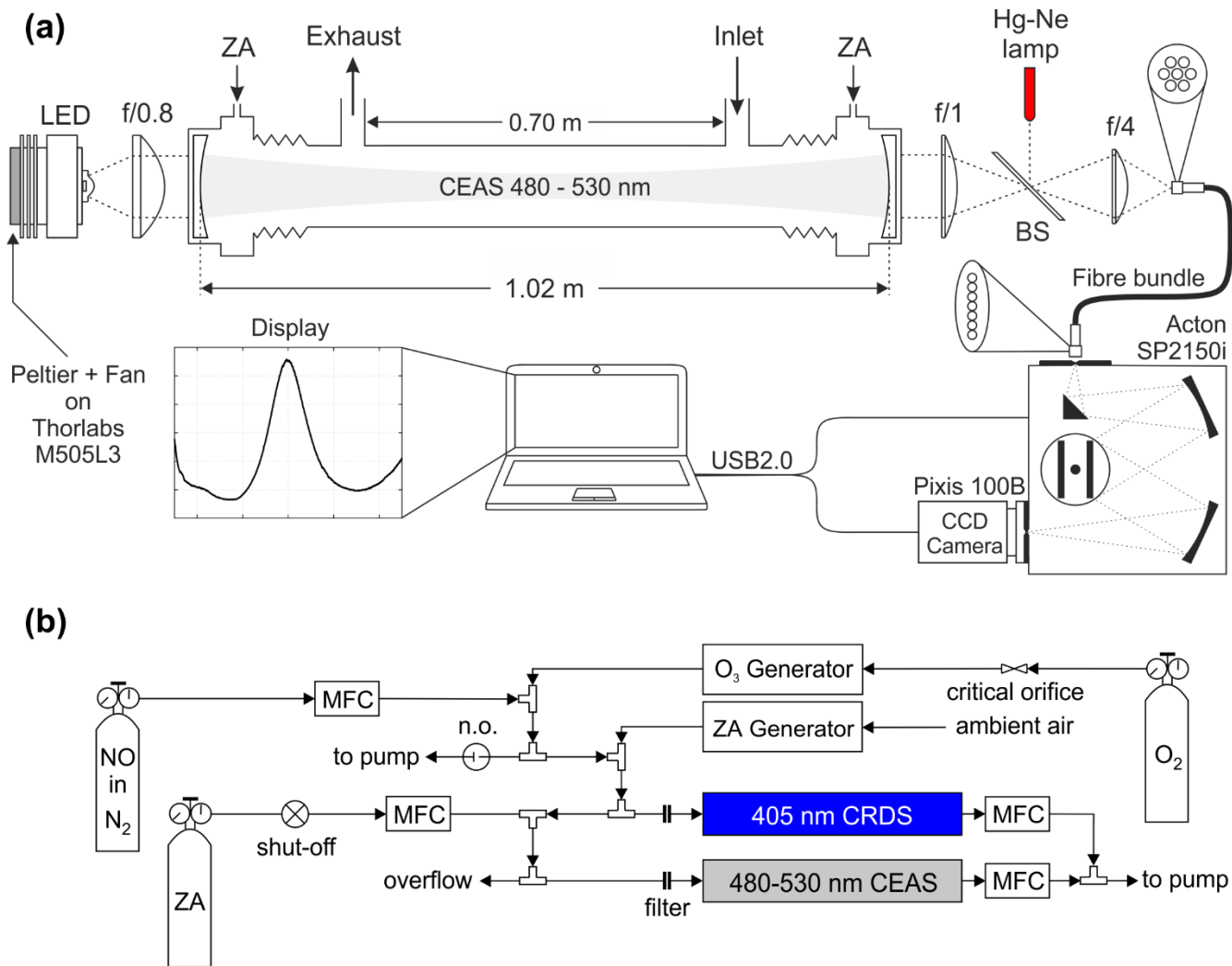
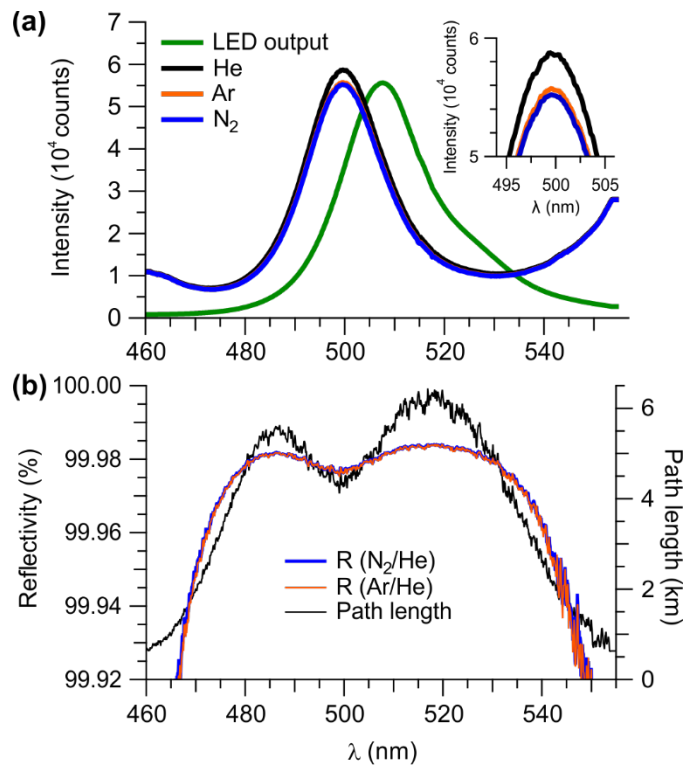
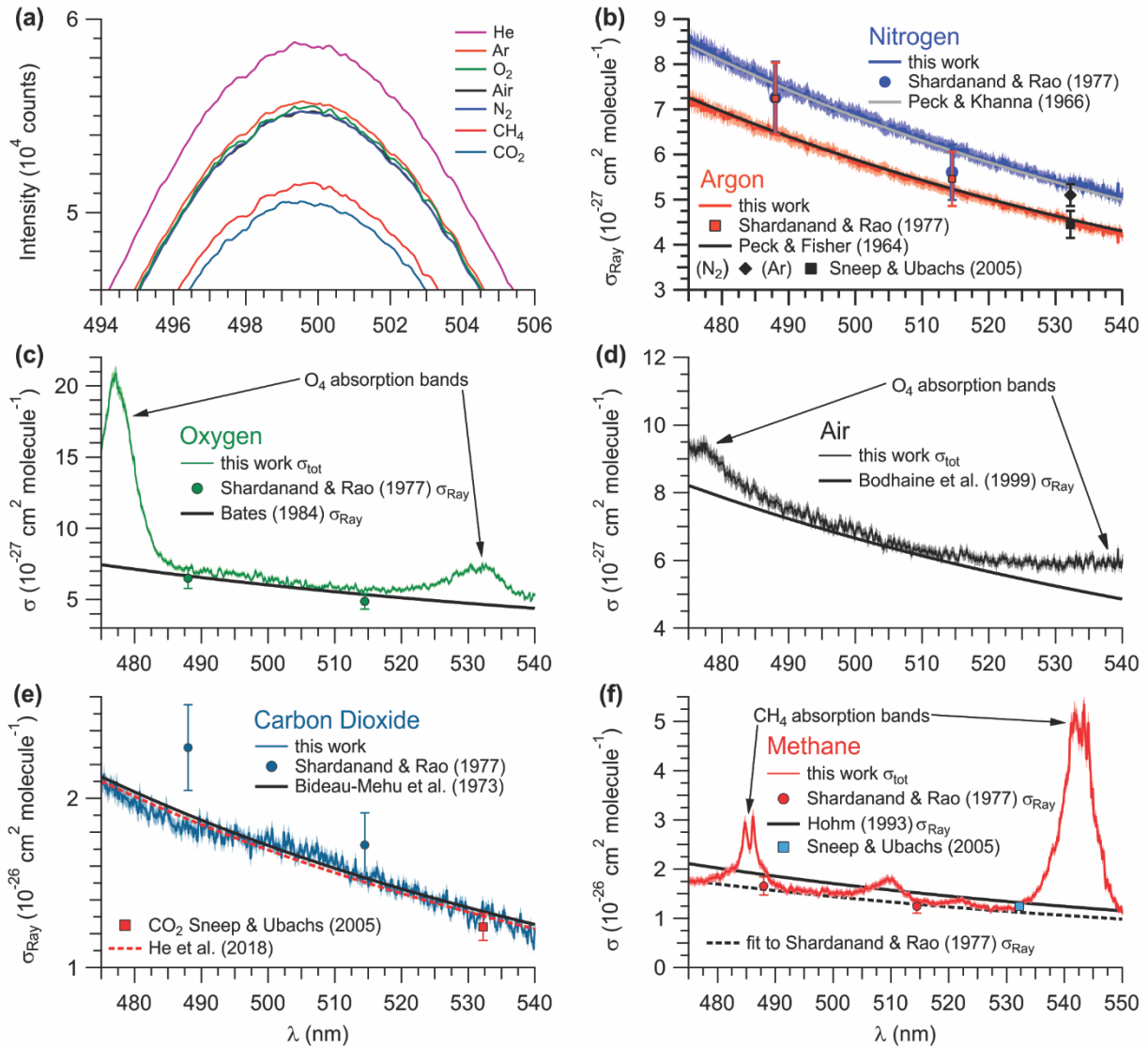


**Figure 2.** (a) Setup of the cyan IBBCEAS (not to scale). (b) Setup of  $\text{NO}_2$  calibration gas delivery for instrument characterization experiments. Abbreviations: LED – light emitting diode, BS – quartz beam splitter, CCD – charge-coupled device, ZA – zero air, USB – universal serial bus, and MFC – mass flow controller.



750

**Figure 3. (a):** Transmission spectra (averaged over 15 min) observed when the sample cell was filled with He, Ar, or N<sub>2</sub> at ambient pressure (890 hPa). The LED output spectrum (in arbitrarily scaled units) is superimposed. **(b):** Mirror reflectivity and effective path length (based on Ar/He) calculated from the data shown in panel (a).



755 **Figure 4.** Measurements of pure gases. (a) Relative intensities of the IBBCEAS signal due to each sampled gas. Extinction cross-sections of (b) 99.998% N<sub>2</sub> (shown in blue) and 99.998% Ar (red), (c) air (black), (d) 99.99% O<sub>2</sub> (green), (e) 99.95% CO<sub>2</sub> (teal), and (f) 99.97% CH<sub>4</sub> (red). Shaded areas represent  $\pm 2.5\%$  error margin in N<sub>2</sub>, Ar, O<sub>2</sub>, air, and CO<sub>2</sub>, and 4.6% in CH<sub>4</sub>.  $\sigma_{\text{Ray}}$  - Rayleigh scattering cross-section;  $\sigma_{\text{tot}}$  = total extinction cross-section ( $=\sigma_{\text{Ray}} + \sigma_{\text{abs}}$ ).

760

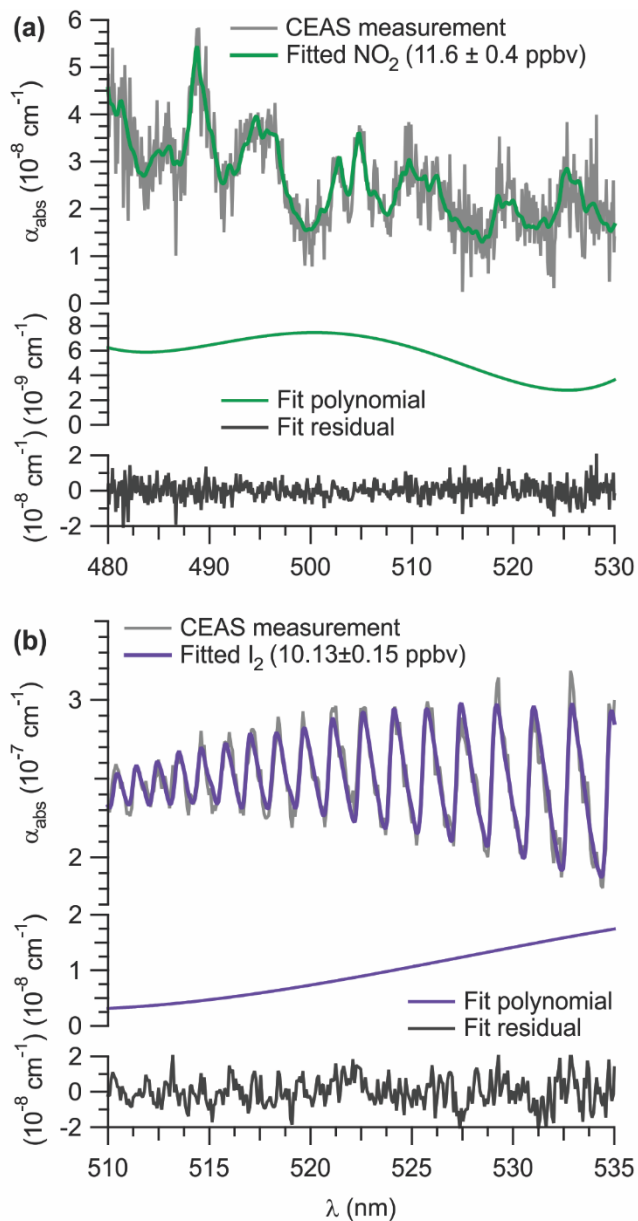
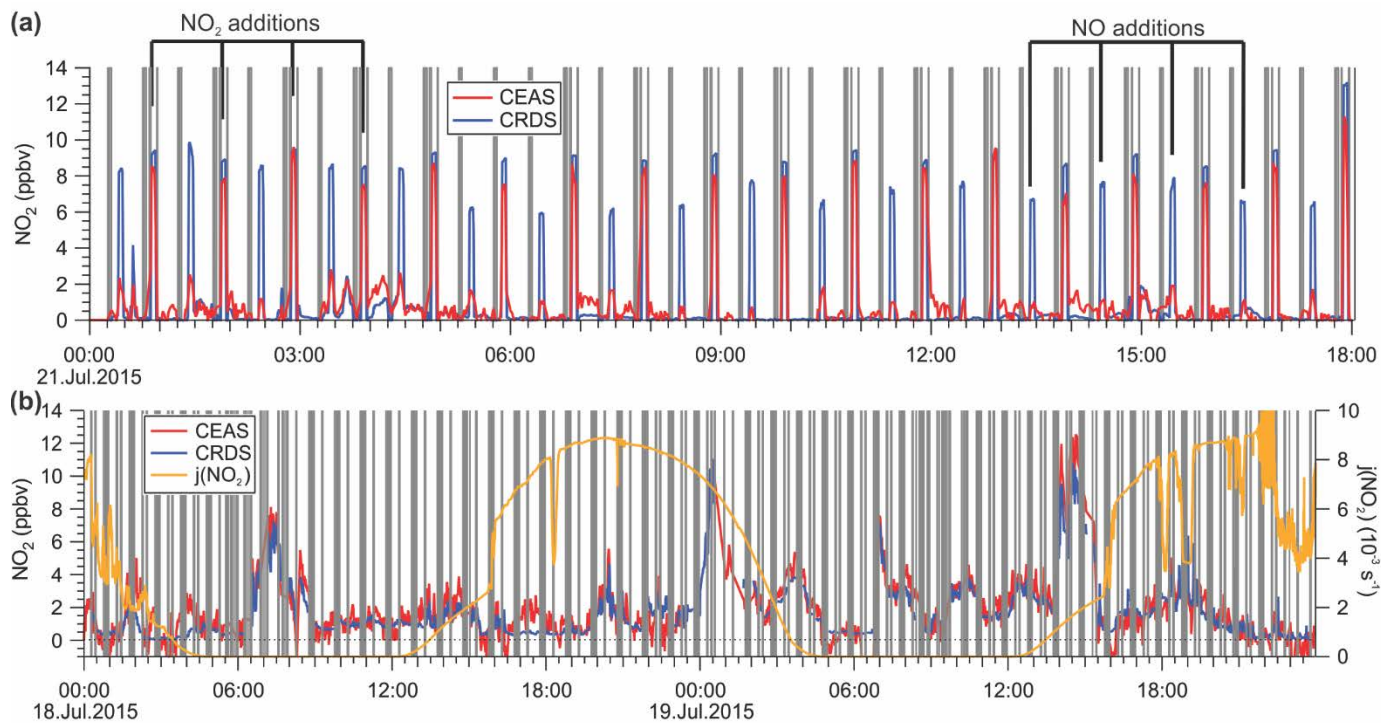


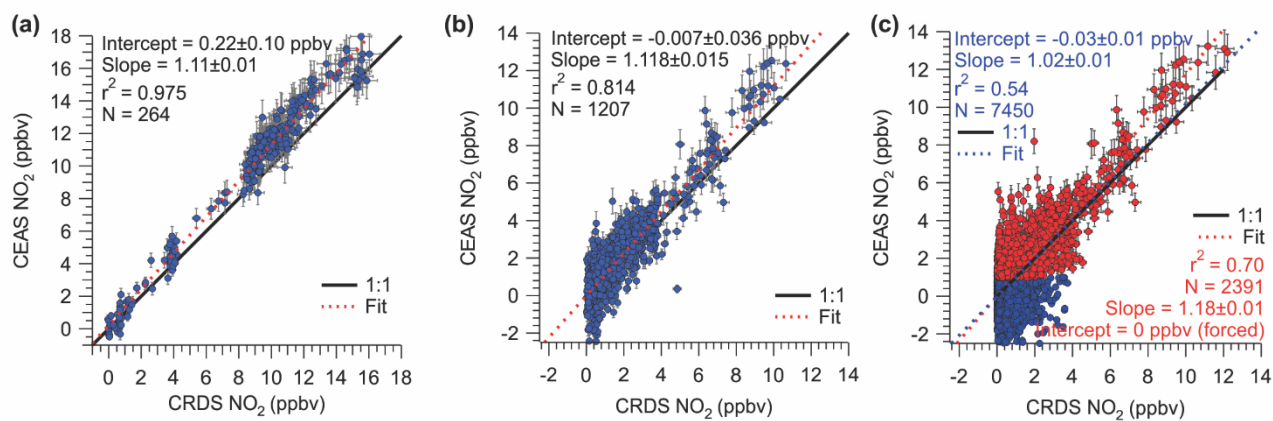
**Figure 5.** Spectral fits to 60 s IBBCEAS signal, including a 3<sup>rd</sup> order polynomial and fit residual, for **a)**  $\text{NO}_2$  (ambient) and **b)**  $\text{I}_2$  (calibration) during the ORCA field campaign.



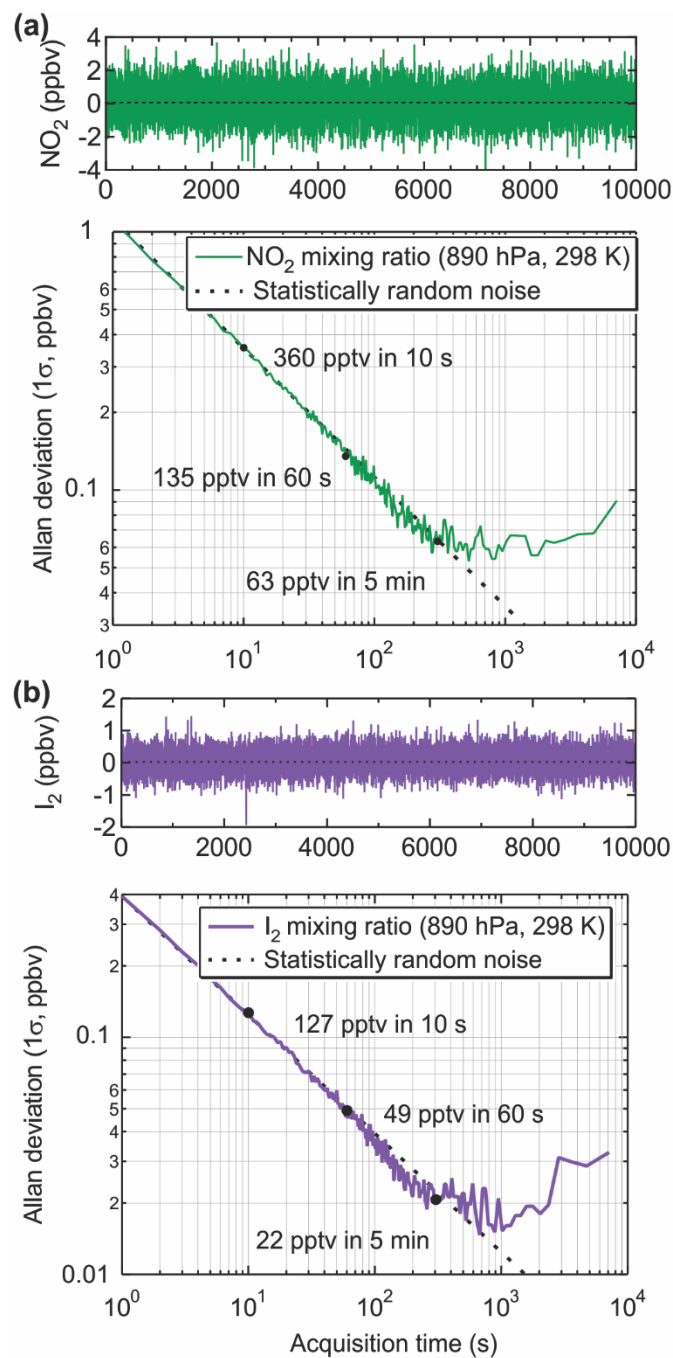
765

**Figure 6.** (a) Sample time series of continuous IBBCEAS and CRDS data collected during the ORCA campaign showing measurements of ambient air, NO<sub>2</sub>-free "zero" air (every 30 min), and hourly standard additions of NO<sub>2</sub> (~10 ppbv) in "zero air" and NO (~130 ppbv) to ambient air. The areas shaded in grey indicate times when both instruments sampled zero air. When high concentrations of NO were added, more NO<sub>2</sub> was observed by CRDS due to this instrument's longer inlet residence time. (b) Sample time series of ambient air NO<sub>2</sub> mixing ratios observed by IBBCEAS and CRDS during ORCA.

770



775 **Figure 7.** Scatter plots and straight-line fits of IBBCEAS and CRDS NO<sub>2</sub> mixing ratios for: **(a)** standard additions and calibrations, **(b)** ambient air measurements on 18-19 Jul 2015, and **(c)** ambient air measurements of the entire campaign. For the fit line shown in red, IBBCEAS retrievals with NO<sub>2</sub> mixing ratios <1 ppbv were excluded. All data were averaged to 60 s.



780

**Figure 8.** Allan deviation plots of data collected while the IBBCEAS was sampling zero air to determine the optimum integration time of: **(a)** the calculated NO<sub>2</sub> mixing ratios at 890 hPa (1.5 slpm sample rate) and 298 K, and **(b)** the calculated I<sub>2</sub> mixing ratios under the same conditions.

**Table 1.** Summary of observed and  $n$ -based Rayleigh scattering cross-sections.

Gas (Purity)	$\lambda$ (nm)	$\sigma_{Ray}$ (this work) <sup>a</sup> ( $10^{-27}$ cm <sup>2</sup> molecule <sup>-1</sup> )	$\sigma_{Ray}$ ( $n$ -based) <sup>b</sup> ( $10^{-27}$ cm <sup>2</sup> molecule <sup>-1</sup> )	$\sigma_{Ray}$ (CRDS) <sup>d</sup> ( $10^{-27}$ cm <sup>2</sup> molecule <sup>-1</sup> )	( $n-1$ ) $\times 10^{-6}$	$F_k^c$
N <sub>2</sub> (99.998%)	485.03	7.85	7.74	-	284.97	1.034
	495.08	7.16	7.12	-	284.70	
	505.01	6.61	6.56	-	284.45	
	515.06	6.09	6.06	-	284.22	
	525.07	5.61	5.60	-	283.99	
	532.20	5.49	5.30	5.1( $\pm 0.2$ )	283.84	
O <sub>2</sub> (99.99%)	485.03	-	6.83	-	273.34	1.096
	495.08	6.84	6.28	-	273.03	
	505.01	5.96	5.78	-	272.74	
	515.06	5.72	5.33	-	272.46	
	525.07	-	4.93	-	272.21	
Air <sup>e</sup>	485.03	-	7.54	-	279.38	1.133
	495.08	7.22	6.93	-	279.10	
	505.01	6.60	6.39	-	278.84	
	515.06	6.04	5.89	-	278.59	
	525.07	-	5.45	-	278.36	
Ar (99.998%)	485.03	6.58	6.67	-	269.02	1.000
	495.08	6.10	6.13	-	268.77	
	505.01	5.61	5.65	-	268.54	
	515.06	5.19	5.22	-	268.31	
	525.07	4.81	4.82	-	268.11	
	532.20	4.40	4.56	4.4 ( $\pm 0.3$ )	267.97	
CO <sub>2</sub> (99.97%)	485.03	19.0	19.5	-	429.81	1.136
	495.08	18.0	17.9	-	429.33	
	505.01	16.9	16.5	-	428.88	
	515.06	14.7	15.2	-	428.46	
	525.07	13.7	14.1	-	428.06	
	532.20	13.9	13.3	12.4( $\pm 0.8$ )	427.79	
CH <sub>4</sub> (99.95%)	492.06	15.4	15.4 <sup>f</sup>	-	483.22	1.000
	497.46	14.7	14.7 <sup>f</sup>	-	482.87	
	501.72	14.5	14.2 <sup>f</sup>	-	482.59	
	516.92	12.8	12.6 <sup>f</sup>	-	481.66	
	527.28	11.6	11.7 <sup>f</sup>	-	481.08	
	532.20	13.1	13.2 <sup>f</sup>	12.5( $\pm 0.2$ )	480.81	

<sup>a</sup> The absolute uncertainty is  $\pm 2.5\%$  (see Sect. 4.1); <sup>b,c</sup> See text for references of  $n$ -based scattering cross-sections and references therein for corresponding calculations of King (King, 1923) correction factors; <sup>d</sup> From (Sneep and Ubachs,

2005); uncertainty is stated as  $1\sigma$ . <sup>e</sup>The ratio of  $N_2/O_2$  in the cylinder was  $\sim 80.5/19.5$ ; <sup>f</sup> Comparison is to the fitted expression to the data set of (Shardanand and Rao, 1977).

790

**Table 2.** Selected CEAS detectors for quantification of NO<sub>2</sub> in the near-UV and visible region of the electromagnetic spectrum

	Arc 330 (Washenfelde r et al., 2016)	Violet 365 (Gherman et al., 2008)	Blue 455 (Min et al., 2016)	Blue 455 (Langridge et al., 2006)	Blue 465 (Thalman and Volkamer, 2010)	Red 643 (Triki et al., 2008)	Red 660 (Wu et al., 2014)	Cyan 508 (This work)
Light source manu-facturer	Energetiq	Omicron Latronics	LEDEngin	Lumileds Luxeon	LEDEngin	Lumileds Luxeon	Marubeni America	Thorlabs
model	Laser-driven arc lamp	n/a	LZ1-00DB05	LXHL-PR09	LZ1-00DB05	LXHL- MD1D	SMB660N- 1100	M505L3
optical power (W)	125 W	0.105	1	0.450	1.0	0.190	0.300	0.440
$\lambda_p \pm \text{FWHM}^a$ (nm)	n/a	365±12	460±5	455±20	465±22	643±20	660±14	508±30
Fit range(s) (nm)	315-350	366 – 378	438 – 468	441 – 463	435 – 465 455 – 487	640 – 670	353 – 376	480 – 530
Mirror reflectivity (%)	99.93	99.94	99.997	99.976	99.9964	99.991	99.925	99.9998
Cell length (m)	1.00	1.15 and 4.50	0.48	1.50	0.99	2.00	1.76	1.02
Path length <sup>b</sup> (km)	1.43	1.9 and 7.5	17.8	6.25	27.5	22	2.1	510
Integration time (s)	30	600	5	30	60	60	120	60
LOD (1 $\sigma$ , ppbv)	0.14 <sup>#</sup>	0.38*	0.04 <sup>#</sup>	0.10*	0.030	9.0*	1	0.14* 0.53 <sup>#</sup>

<sup>a</sup> peak wavelength + full-width at half maximum; <sup>b</sup> effective path length,  $L_{\text{eff}} = 1/(1-R)$ ; \* laboratory sample; # field samples